

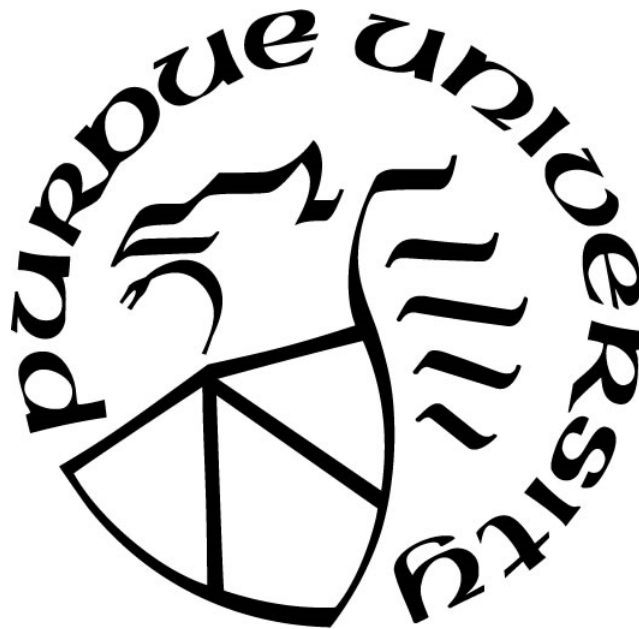
# AERODYNAMIC HEATING IN MISSILE-FIN GAP REGION

by  
Devon Fano

A Thesis

*Submitted to the Faculty of Purdue University  
In Partial Fulfillment of the Requirements for the degree of*

**Master of Science in Aeronautics and Astronautics**



School of Aeronautics and Astronautics  
West Lafayette, Indiana  
August 2020

**THE PURDUE UNIVERSITY GRADUATE SCHOOL  
STATEMENT OF THESIS APPROVAL**

Dr. Jonathan Poggie, Chair

School of Aeronautics and Astronautics

Dr. Gregory Blaisdell

School of Aeronautics and Astronautics

Dr. Joseph Jewell

School of Aeronautics and Astronautics

**Approved by:**

Dr. Gregory Blaisdell

Head of the School Graduate Program

## ACKNOWLEDGMENTS

Thank you to my advisor, Dr. Jonathan Poggie, for providing support throughout all phases of graduate school and for offering me the opportunity to be a part of his research team. He has been a great mentor and the experience of working in his group has taught me numerous lessons that I believe will always prove valuable. I would also like to thank my co-advisor, Dr. Gregory Blaisdell, for helping guide my understanding of aerodynamics and for contributing many key insights to this research. In addition, thank you to Dr. Joseph Jewell for being a member of my committee and for offering helpful feedback needed to complete this thesis.

The presented work was supported by the Air Force Research Lab under contract FA8650-18-C-2253 with program manager J. Boston. All material shown was assigned a clearance of CLEARED (case number 88ABW-2020-2378) on July 26, 2020. Computational resources were provided by the Department of Defense Supercomputing Resource Centers and by Information Technology at Purdue University, West Lafayette, Indiana.

## TABLE OF CONTENTS

	Page
LIST OF TABLES . . . . .	v
LIST OF FIGURES . . . . .	vi
SYMBOLS . . . . .	viii
ABBREVIATIONS . . . . .	ix
ABSTRACT . . . . .	x
1 Introduction . . . . .	1
1.1 Shock Wave/Boundary Layer Interactions . . . . .	2
1.2 Heat Transfer . . . . .	4
1.3 Scope of Research . . . . .	6
2 Methodology . . . . .	9
2.1 Experimental Background . . . . .	9
2.2 Mesh Generation . . . . .	14
2.2.1 Baseline Configuration . . . . .	15
2.2.2 Missile-Fin Configuration . . . . .	17
2.2.3 Classification of Meshes . . . . .	19
2.3 Simulation Configuration . . . . .	21
2.4 Computational Resources . . . . .	22
2.5 Parametric Study Overview . . . . .	23
3 Baseline Results . . . . .	25
3.1 Solution Convergence . . . . .	25
3.2 Grid Resolution Study . . . . .	26
3.3 Overall Flow Structure . . . . .	27
3.4 Heat Transfer . . . . .	29

	Page
4 Missile-Fin Results . . . . .	38
4.1 Solution Convergence . . . . .	38
4.2 Overall Flow Structure . . . . .	40
4.3 Heat Transfer . . . . .	41
5 Conclusions . . . . .	55
REFERENCES . . . . .	58
A Model Dimensioned Drawings . . . . .	60
B Derivation of Equation 2.4 . . . . .	61
C Stagnation Point Heating . . . . .	62

## LIST OF TABLES

Table	Page
2.1 Freestream Flow Conditions . . . . .	10
2.2 Baseline Mesh Point Counts . . . . .	16
2.3 Missile-Fin Mesh Cylinder and Total Point Counts . . . . .	18
2.4 Simulation Settings . . . . .	22
2.5 Parametric Study Outline . . . . .	24

## LIST OF FIGURES

Figure	Page
1.1 Shock Wave Temperature-Contour Plot . . . . .	4
1.2 Temperature Profile Above Heated Surface . . . . .	6
2.1 Simulated Missile-Fin Configuration Depiction . . . . .	11
2.2 Missile Model Coordinate System . . . . .	11
2.3 Baseline Mesh - Coarse . . . . .	15
2.4 Fin Bottom Surface Grid . . . . .	18
2.5 Missile-Fin Mesh . . . . .	19
2.6 Baseline Base Grid - Coarse . . . . .	20
3.1 Missile Model Coordinate System (Repeated) . . . . .	30
3.2 Baseline Solution Convergence - Surface Pressure . . . . .	30
3.3 Baseline Solution Convergence - $C_{fx}$ . . . . .	31
3.4 Baseline Solution Convergence - $\dot{q}$ . . . . .	31
3.5 Baseline Grid Resolution Study - $y^+$ - $\alpha = 0^\circ, -4^\circ$ . . . . .	31
3.6 Baseline Grid Resolution Study - $y^+$ - $\alpha = -8^\circ, -12^\circ$ . . . . .	32
3.7 Baseline Grid Resolution Study - Surface Pressure . . . . .	32
3.8 Baseline Grid Resolution Study - $C_{fx}$ . . . . .	32
3.9 Baseline Grid Resolution Study - $\dot{q}$ . . . . .	33
3.10 Baseline Mach-Contour Plot - $\alpha = 0^\circ$ . . . . .	33
3.11 Baseline Mach-Contour Plot - $\alpha = -4^\circ$ . . . . .	33
3.12 Baseline Mach-Contour Plot - $\alpha = -8^\circ$ . . . . .	34
3.13 Baseline Mach-Contour Plot - $\alpha = -12^\circ$ . . . . .	34
3.14 Baseline Circumferential Surface Pressure - M.S. 107 - $\alpha = -4^\circ, -8^\circ$ . . . . .	35
3.15 Baseline Boundary Layer $P_T$ Profile - M.S. 107 - $\alpha = 0^\circ, -4^\circ$ . . . . .	35
3.16 Baseline Boundary Layer $P_T$ Profile - M.S. 107 - $\alpha = -8^\circ, -12^\circ$ . . . . .	35

Figure	Page
3.17 Baseline Boundary Layer Thickness - M.S. 107 . . . . .	36
3.18 Baseline Shock Wave $P_T$ Profile - M.S. 107 - $\alpha = -4^\circ, -8^\circ$ . . . . .	36
3.19 Baseline Circumferential $h$ - M.S. 89 - $\alpha = 0^\circ, -4^\circ$ . . . . .	36
3.20 Baseline Circumferential $h$ - M.S. 89 - $\alpha = -8^\circ, -12^\circ$ . . . . .	37
3.21 Baseline Maximum $h$ - M.S. 89 . . . . .	37
4.1 Gap Region Coordinate System . . . . .	44
4.2 Missile-Fin Solution Convergence - Surface Pressure - $g_h = 0.508$ cm, 0.762 cm	44
4.3 Missile-Fin Solution Convergence - Surface Pressure - $g_h = 1.016$ cm, 1.270 cm	44
4.4 Missile-Fin Solution Convergence - $C'_{fx}$ - $g_h = 0.508$ cm, 0.762 cm . . . . .	45
4.5 Missile-Fin Solution Convergence - $C'_{fx}$ - $g_h = 1.016$ cm, 1.270 cm . . . . .	45
4.6 Missile-Fin Solution Convergence - $\dot{q}$ - $g_h = 0.508$ cm, 0.762 cm . . . . .	45
4.7 Missile-Fin Solution Convergence - $\dot{q}$ - $g_h = 1.016$ cm, 1.270 cm . . . . .	46
4.8 Missile-Fin Mach-Contour Plot - $\alpha = 0^\circ$ . . . . .	46
4.9 Missile-Fin Mach-Contour Plot - $\alpha = -4^\circ$ . . . . .	46
4.10 Missile-Fin Mach-Contour Plot - $\alpha = -8^\circ$ . . . . .	47
4.11 Missile-Fin Mach-Contour Plot - $\alpha = -12^\circ$ . . . . .	47
4.12 Missile-Fin Mach-Contour Plot with Streamlines . . . . .	48
4.13 Missile-Fin Surface Pressure - $\alpha = 0^\circ, -4^\circ$ . . . . .	48
4.14 Missile-Fin Surface Pressure - $\alpha = -8^\circ, -12^\circ$ . . . . .	48
4.15 Missile-Fin $C'_{fx}$ - $\alpha = 0^\circ$ . . . . .	49
4.16 Missile-Fin $C'_{fx}$ - $\alpha = -4^\circ$ . . . . .	49
4.17 Missile-Fin $C'_{fx}$ - $\alpha = -8^\circ$ . . . . .	49
4.18 Missile-Fin $C'_{fx}$ - $\alpha = -12^\circ$ . . . . .	50
4.19 Missile-Fin $y^+$ - $g_h = 0.508$ cm, 0.762 cm . . . . .	50
4.20 Missile-Fin $y^+$ - $g_h = 1.016$ cm, 1.270 cm . . . . .	50
4.21 Missile-Fin $h$ Distribution - $g_h = 0.762$ cm - $\alpha = 0^\circ, -4^\circ$ . . . . .	51
4.22 Missile-Fin $h$ Distribution - $g_h = 0.762$ cm - $\alpha = -8^\circ, -12^\circ$ . . . . .	51
4.23 Missile Fin $h$ - $\alpha = 0^\circ, -4^\circ$ . . . . .	51

Figure	Page
4.24 Missile Fin $h$ - $\alpha = -8^\circ, -12^\circ$ . . . . .	52
4.25 Missile-Fin Missile Surface Maximum $h$ . . . . .	52
4.26 Missile-Fin Missile Surface Maximum $h$ Experimental Data . . . . .	53
4.27 Missile-Fin Heating-Contour Plot - $g_h = 0.762$ cm - $\alpha = 0^\circ$ . . . . .	53
4.28 Missile-Fin Heating-Contour Plot - $g_h = 1.016$ cm - $\alpha = -12^\circ, g_h = 1.270$ cm - $\alpha = -4^\circ$ . . . . .	54
4.29 Missile-Fin Cylinder Surface Maximum $h$ . . . . .	54
A.1 Dimensions of Simulated Missile and Fin Models . . . . .	60

## SYMBOLS

$C_{fx}$	Streamwise skin friction coefficient
$g_h$	Gap height
$h$	Heat transfer coefficient
M.S.	Model station
$P_T$	Pitot pressure
$\dot{q}$	Heat flux
$T_R$	Recovery temperature
$T_W$	Wall temperature
X/D	Cylinder diameter lengths upstream of cylinder surface
$y^+$	Non-dimensional wall distance
$\alpha$	Angle of attack
$\gamma$	Ratio of specific heat at constant pressure to constant volume
$\delta$	Boundary layer thickness
$\Delta s$	First cell wall-normal grid spacing
$\mu$	Dynamic viscosity
$\phi$	Angular coordinate

*Subscripts*

$\infty$	Freestream
0	Stagnation

## ABBREVIATIONS

AFRL	Air Force Research Laboratory
ARL	Army Research Laboratory
CAD	Computer-aided design
CFD	Computational fluid dynamics
DoD	Department of Defense
ERDC	Engineer Research and Development Center
PBS	Portable batch system
RANS	Reynolds-averaged Navier-Stokes
SI	Système international
SSH	Secure shell
SWBLI	Shock wave/boundary layer interactions

## ABSTRACT

Fano, Devon MS, Purdue University, August 2020. Aerodynamic Heating in Missile-Fin Gap Region. Major Professor: Jonathan Poggie.

Large heat transfer rates are a major source of possible failure in flight vehicles due to increases in temperature being linked to weakening material properties. Aircraft in high-Mach number flow generate excessive aerodynamic heat that may increase temperatures above limits of structural integrity. Even without reducing speed or changing material, it is possible to mitigate heat transfer by altering vehicle geometry. The purpose of this thesis is to study the extent of heat transfer in gap regions of various sizes by computationally simulating flow over an idealized missile-fin configuration. Maximum levels of heat transfer are analyzed as well as surface distributions that identify key design points. The Department of Defense software package with computational fluid dynamics capabilities, Kestrel, was employed to use the Reynolds-averaged Navier-Stokes equations to simulate turbulent Mach 6 flow over the missile model. Results are compared to data obtained by the Air Force Research Laboratory via wind tunnel tests of the same flow. Experiments and simulations both found an order of magnitude increase in heat transfer when an offset fin was attached, but this heating could be reduced by minimizing the offset distance. Simulated baseline properties agreed very well with experimental measurements and simulations of the gap region more precisely identified the locations of maximum heating.

## 1. INTRODUCTION

Research on high-Mach number flow has been conducted for at least a half-century. Since the 1960's, wind tunnels capable of reaching Mach 5 and greater have been utilized to gather data that have influenced the construction of missiles and re-entering spacecraft. Yet, as their top speeds and design complexities have increased over the years, modern flight vehicles are costly to analyze in wind tunnels under realistic flight conditions. High-performance computers have therefore become attractive as tools for simulating flow over aircraft and calculating properties of interest. Lift, drag, and moments are some properties that are required for design and predicted using computational fluid dynamics. In theoretical aerodynamics, other properties, many related to boundary layers, are analyzed using CFD, including skin friction and heat flux. Findings from theoretical aerodynamics can influence practical vehicle design even if the vehicle itself is not involved. Edward van Driest, a 20th century professor, researcher, and engineer who made significant contributions to compressible turbulent flow theory, stated that “[t]wo major problems encountered today in aeronautics are the determination of skin friction and skin temperatures of high-speed aircraft” [1]. Skin temperatures are directly linked to heat transfer, which is the focus of this thesis.

Even without the challenges of wind tunnels, simulations present difficulties. Computers capable of running high-fidelity simulations for long periods of time are costly to build, operate, and maintain. An early step in the CFD process, mesh generation, often requires time-consuming effort by designers. Governing equations of fluid flow are complicated to discretize and the optimal algorithm varies by case. Fortunately, there are many CFD codes available that allow users to choose from included numerical schemes. Also, software programs with graphical user interfaces exist to aid designers in mesh generation. Still, properties of interest can be sensitive to simula-

tion design and the effects of different numerical schemes and mesh details are not fully understood.

This chapter presents an overview of the physics related to high-Mach number flow. Discussion focuses on shock wave/boundary layer interactions (SWBLI), heat transfer, and relevant existing research. It concludes with a section defining the scope of the research for this thesis and a summary of the remaining chapters.

## 1.1 Shock Wave/Boundary Layer Interactions

The boundary layer is a fundamental concept of fluid flow over a surface. First described by Ludwig Prandtl in 1904, the boundary layer is the region of fluid very close to a surface where viscosity significantly slows the flow. Fluid properties, such as velocity, temperature, and density, change rapidly across the boundary layer. Its edge can be defined in multiple ways, but generally it is where flow properties become close to properties far from the boundary layer. Boundary layers can separate in a pressure gradient, where pressure changes along the surface, and boundary layer attributes change depending if flow is laminar or turbulent. Many other factors also influence boundary layers, so their study is complex. However, boundary layers are important to understand because they can have a major impact on flight vehicles. Hopkins et al. state in their article [2] on high-Mach number turbulent boundary layers that “An accurate theory for predicting [high-Mach number] turbulent skin friction is required for meaningful design studies of [high-Mach number] vehicles.” Skin friction, as well as heat transfer, is caused by gradients of fluid properties close to the surface in boundary layers. The partial differential equations that govern boundary layers, though, often lack exact solutions for “practical problems of interest” [3]. One of the earliest approaches to studying boundary layers involves making certain assumptions that rewrite the governing equations as similarity solutions, which are easily solved numerically. With improvements in numerical methods and the advent of computers, modern CFD codes can simulate boundary layers without similarity solutions.

Shock waves are abrupt changes in flow properties that occur when a disturbance travels faster than the local speed of sound. An object in high-Mach number flow will produce a bow shock wave slightly detached from its nose cone that propagates away from its body. The angle of this bow shock wave narrows for higher Mach numbers. Across a shock wave, Mach number, velocity, and stagnation pressure all decrease, while density, pressure, temperature, and entropy all increase. Enthalpy remains constant. Figure 1.1 shows a temperature-contour plot from a simulation modeling flow around a missile at Mach 6. The bow shock wave front is easily discernible as well as the boundary layer on the missile surface. Protrusions from an aircraft and deflections of control surfaces will also produce shock waves. When a shock wave occurs in the same region as a boundary layer, the interaction is referred to as a shock wave/boundary layer interaction (SWBLI). In these interactions, the increased pressure downstream of the shock wave propagates upstream through the subsonic portion of the boundary layer and possibly causes boundary layer separation. In that case, the interaction can be described as involving a point of separation, a recirculation region of counter-rotating flow, and a point of reattachment. Especially in 3D, SWBLI are complex and their study relies heavily on CFD [3]. Their study is important, though, and Délerly et al. wrote in 1986 that “[t]he interactions of a shock-wave with a boundary-layer can have a significant influence on aircraft or missile performance. Drag rise, flow separation, adverse aerodynamic loading, high aerodynamic heating, and poor engine inlet performance are but a few examples of its deleterious influence” [4]. This thesis focuses on the high aerodynamic heating associated with SWBLI.

Most SWBLI studied are those resulting from a set of classical geometric configurations including the swept ramp, single-fin, and double cone. These configurations are useful for research by being both experiment and CFD friendly. A recent article [5] by Gaitonde outlines efforts that have gone into understanding these interactions and details how the accuracies of CFD heat transfer predictions have improved over the years. The article also mentions the severity of SWBLI on vehicles, stating that they

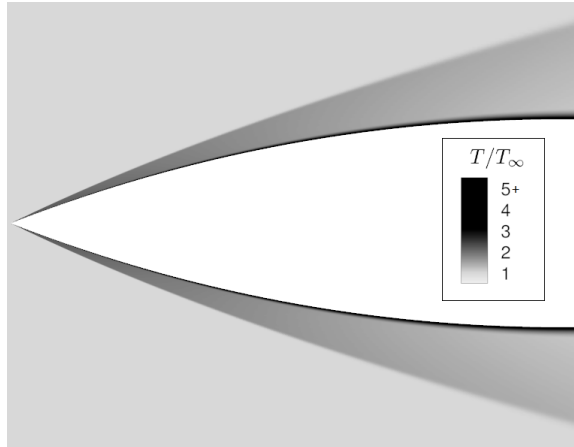


Fig. 1.1. Temperature-contour plot from simulation modeling Mach 6 flow over missile. Freestream properties listed in Table 2.1. Center-plane slice from 3D simulation.

cause “peaks in thermodynamic loading [on the exterior of aircraft].” It also specifies that an “order of magnitude enhancement in heat transfer rates” has been measured in experiments involving the hollow cylinder flare and double-cone. Regarding SWBLI in gaps and cavities, a similar “severe local increase in heating” is known to occur near the flow reattachment point [3]. These studies establish that many classical SWBLI cause excessive heating. The interaction studied for this thesis, a missile-fin juncture flow, resembles the classical interactions and should be expected to produce large rates of heating.

## 1.2 Heat Transfer

Heat transfer refers to the exchange of heat between flow and surfaces. In high-Mach number flow, the abundant kinetic energy manifests itself as a temperature rise in the fluid near the surface through two main processes. First, temperatures increase across the main bow shock wave via compression. Second, temperatures increase in the boundary layer from viscous dissipation [6]. Other shock waves caused by vehicle architecture will also affect heating. If the surface, or wall, temperature  $T_W$  is less

than a certain fluid temperature, heat will flow into the surface. If  $T_W$  is equal to that temperature, thermal equilibrium is achieved and there will be no heat transfer. The temperature that results in thermal equilibrium is the adiabatic wall temperature, or recovery temperature  $T_R$  [7]. Due to viscous effects in the boundary layer,  $T_R$  is less than the freestream stagnation temperature  $T_{0\infty}$ . To describe the relationship between heat transfer and surface temperature, the heat transfer coefficient  $h$  is defined as

$$h = \frac{\dot{q}}{T_{ref} - T_W} \quad (1.1)$$

where  $\dot{q}$  is heat flux and  $T_{ref}$  is a chosen reference temperature. Heat flux is the amount of heat transferred through the wall per unit time and per unit surface area, which has SI units of  $\text{W}/\text{m}^2$ . Heat transfer coefficients change depending on the chosen reference temperature, so  $T_{ref}$  should always be explicitly defined. Common choices for  $T_{ref}$  for high-speed flows are  $T_R$ ,  $T_{0\infty}$ , and a fraction of  $T_{0\infty}$ . The temperature difference  $T_{ref} - T_W$  must be in an absolute temperature unit. Positive values of  $\dot{q}$  represent heat transferring into the wall, and  $h$  is always positive. Heat transfer coefficients have SI units of  $\text{W}/(\text{m}^2\text{K})$ .

In steady flow, the heat transfer coefficient at a specific point is considered constant as wall temperature changes. This assumption means that  $\dot{q}$  is linearly proportional to  $T_{ref} - T_W$ , with  $h$  being the constant of proportionality. Factors that significantly affect  $h$  include boundary layer state, local surface geometry, and shock waves or other flow features. In simulations, these factors all contribute to the gradient of fluid temperature at the wall  $\nabla T_S$ , which can be used to calculate  $\dot{q}$ . Fourier's law can be used to state that

$$\dot{q} = \kappa \nabla T_S \quad (1.2)$$

where  $\kappa$  is the thermal conductivity of the fluid and  $\nabla T_S$  is the change in fluid temperature per unit distance directly above the surface [1]. To show  $\nabla T_S$ , Figure 1.2 plots a generic temperature profile directly above a surface that is being heated by the flow. The dotted line represents  $\nabla T_S$ . To model thermal conductivity, CFD codes can employ thermochemistry relations to calculate  $\kappa$  as a function of fluid temperature.

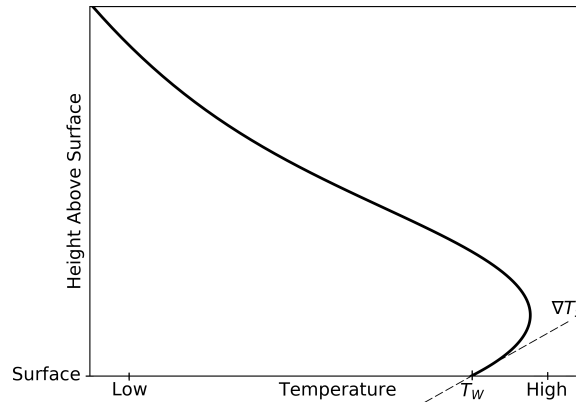


Fig. 1.2. Generic temperature profile above surface being heated. Dashed line represents  $\nabla T_s$ .

### 1.3 Scope of Research

This research aims to expand knowledge of simulating heat transfer in high-Mach number SWBLI. The ability to accurately calculate heat transfer is pertinent and valuable for modern aircraft design. Results from this research also expand on experimental data.

The objective of this thesis is to computationally analyze experiments reported in a technical report [8] by AFRL engineers Richard D. Neumann and James R. Hayes. Their wind tunnel experiments at Mach 6 produced measurements of heat transfer coefficients on an ogive-missile model with an attached fin. They found significant heating in the gap region of the missile-fin configuration and this thesis aims to investigate that heating. A summary of the relevant parts of that technical report is presented in Section 2.1. In formulating the computations carried out for this thesis, details of those experiments were carefully considered. The flow properties, missile model geometry, and most parameters for a parametric study were matched. The report's ample data set on the undisturbed missile model, with no fin, serves to validate simulation methodology. The undisturbed missile model, with no fin, is referred to as the baseline configuration here. Properties of the baseline configuration, such as heat transfer, boundary layer profile, and surface pressure, are simulated and

compared to experimental data. Beyond replicating experimental data, this thesis explores an area of heating in the gap region of the missile-fin configuration that was outside of thermocouple placement. This thesis intends to expand the technical report's conclusions.

Designing simulations involves both mesh generation and selection in numerical methods. A majority of the time spent on this thesis went towards mesh generation. Detailed descriptions of meshes utilized as well as explanations of their construction are presented in Section 2.2. Each of the baseline and missile-fin meshes has its own section; the latter of which required a more intensive design process. Multiple meshing techniques were explored throughout the process and many details were tweaked. This section also includes a discussion on mesh classification.

An outline of the simulation configuration is presented in Section 2.3. The DoD software package Kestrel was utilized to numerically solve the RANS equations and simulate turbulent Mach 6 flow over the missile model. Over the course of research, several solver options were tested and final decisions were made based on agreement with experimental data, suggestions from outside research, and recommendations from Kestrel developers. Simulation specifications remained as constant as possible throughout the set of simulations for the baseline and missile-fin configurations.

The computational resources that ran the presented simulations are summarized in Section 2.4. Resources from Information Technology at Purdue's (ITaP) Rosen Center for Advanced Computing (RCAC) were utilized in the initial stages of learning CFD, but all simulations for this project were executed using the DoD's AFRL, ARL, and ERDC High-Performance Computing (HPC) clusters. Due to relatively large point counts, presented simulations required the substantial computing power of the DoD systems to be completed in a reasonable amount of time.

Simulated results are presented and compared to experimental data in Chapters 3 and 4. Each of the baseline and missile-fin configurations has its own chapter that includes sections pertaining to solution convergence, flow structure, and heat transfer.

A grid resolution study is also included for the baseline configuration. Wherever possible, experimental data are plotted along with simulated properties for comparison.

Conclusions are presented in Chapter 5. The extent of heating in the gap region of the missile-fin configuration is discussed with a focus on its level of increase from the baseline configuration. Trends observed from the parametric study are summarized and agreements with experimental data are listed. Finally, ideas for future investigation are proposed and a possible alternative grid generation approach is recommended.

## 2. METHODOLOGY

This chapter begins with a summary of the experimental study that guided the simulations for this thesis. Then, the simulation process is explained through discussions of mesh generation and CFD configuration. Sections describing mesh classification and computational resources are also included. Last, the cases in the parametric study are summarized in a table.

### 2.1 Experimental Background

A technical report [8] by engineers Richard D. Neumann and James R. Hayes serves as the experimental background for this thesis. In the late 1970's, Neumann and Hayes ran a multitude of Mach 6 wind tunnel tests at the Arnold Engineering Development Center using Tunnel B. The tests involved flow over an idealized missile model. Freestream flow conditions were identical for all relevant tests and are listed in Table 2.1. All units in the technical report are non-SI, so for simplicity every value is converted to SI in this thesis. The only freestream flow inputs to the simulations were  $M_\infty$ ,  $T_{0\infty}$ , and  $P_{0\infty}$ . The simulated air was considered calorically perfect, so all other properties are computed using isentropic flow relations, the definition of Reynolds number, the ideal gas law, the speed of sound, or Sutherland's law. Note, the isentropic relation for  $T_0$  only requires an adiabatic assumption [9].

Neumann and Hayes's experiments involved a 1.27 m long stainless steel ogive-cylinder idealized missile model. The ogive section at the front extended for 57.2 cm and the base diameter was 21.6 cm. Initial testing involved the plain missile configuration, with no fin, which is called the baseline configuration in this thesis. With fin attached, the setup will be called the missile-fin configuration. The missile-fin configuration is shown in Figure 2.1. The geometry of the fin varied slightly between

Table 2.1.  
Freestream Flow Conditions

$M_\infty$	5.95	
$T_{0\infty}$	461.1	K
$P_{0\infty}$	$1.724 \times 10^6$	Pa
$u_\infty$	900.1	m/s
$T_\infty$	57.06	K
$P_\infty$	1149	Pa
$\rho_\infty$	0.07017	kg/m <sup>3</sup>
$\mu_\infty$	$3.753 \times 10^{-6}$	Pa·s
$Re_\infty$	$1.685 \times 10^7$	/m

the one in the wind tunnel tests and the one simulated. The one in the wind tunnel tests had four triangular faces and no top face. The simulated fin is 15.2 cm long, has triangular side faces, a triangular top face, and is situated toward the rear of the missile model with its tip located at M.S. 107. Model station M.S. represents the distance in centimeters from the missile tip along the center axis. Points on the missile model range from M.S. 0 to M.S. 127. A cylinder, also called a torque tube by the experimenters, connected the fin to the missile model. The cylinder's diameter was 1.59 cm and it was centered at M.S. 117. The gap, with gap height  $g_h$ , between the missile and fin would allow the fin to rotate as a control surface in a real air vehicle. Data were reported for gap heights that ranged from 0.254 cm to 1.016 cm. Dimensioned drawings of the simulated missile and fin models are given in the Appendix.

Wind tunnel tests involved the model pitched at various angles of attack  $\alpha$  and measurements were taken at multiple model stations and angular coordinates  $\phi$ . The model was only pitched downward, so  $\alpha$  is always zero or negative. The angle  $\phi$  is measured from  $0^\circ$  to  $180^\circ$  with  $0^\circ$  representing the centerline of the windward, or top,

side of the missile model. Figure 2.2 depicts this coordinate system. Experimentally tested angles of attack ranged from  $0^\circ$  to  $-12^\circ$ . Neumann and Hayes also experimented with various roll angles for the missile-fin configuration, but simulations for this thesis only involved roll angles of  $0^\circ$ .

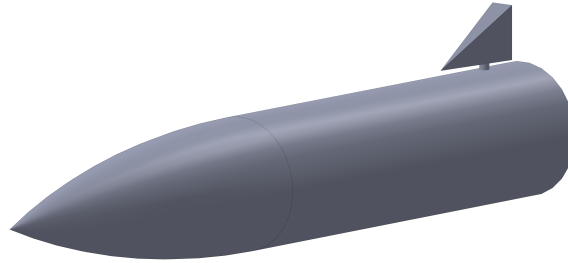


Fig. 2.1. Simulated missile-fin configuration. Baseline configuration has no fin.

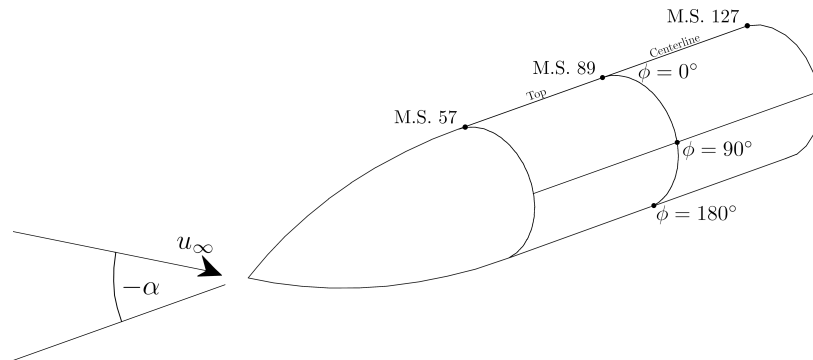


Fig. 2.2. Missile model coordinate system.

Thermocouples and pressure transducers were used to take measurements. The thermocouples were installed in thin-skin metal inserts with thickness 0.762 mm. At the location of a thermocouple, two wires were welded through small holes in the thin-skin insert at a spacing of also 0.762 mm. A temperature-dependent voltage arose in the metal from the thermoelectric effect and the voltage measurements were converted to temperature measurements. The model was cooled using high-pressure air between tests until all thermocouples measured less than 303 K and differed by less than 6 K. During tests, which each lasted about 4 seconds, thermocouple readings were recorded

every 0.06 seconds. Calculating  $h$  from thermocouple data was accomplished using an equation similar to Equation 1.1. The known specific heat capacity of the metal was used to calculate heat flux, which is equal to

$$\dot{q} = \frac{C_p \rho w \Delta T}{\Delta t} \quad (2.1)$$

where  $C_p$  is the specific heat capacity of the thin-skin insert metal,  $\rho$  is the density of the metal,  $w$  is the thickness of the thin-skin insert,  $\Delta T$  is the change in temperature, and  $\Delta t$  is the change in time. Radiation effects were considered negligible and ignored, but conduction effects were noted to be an issue. Neumann and Hayes developed a data reduction method to identify and account for conduction effects, and they report the overall uncertainty in  $h$  to be between 6% and 7%. To measure pressure, a large Pitot probe rake was constructed to probe the main bow shock wave and a small Pitot probe rake was constructed to probe the boundary layer. The spacing of probes in the large rake was 2.54 cm and the spacing in the small rake was 0.254 cm. However, using radial displacement techniques, the effective spacing in the large rake was 0.635 cm. The same type of pressure transducer used in the Pitot rakes was also placed on the missile model to measure surface pressure. All pressure measurements were referenced to near vacuum, and their overall uncertainties were reported as about 0.2%.

Neumann and Hayes gathered data for the baseline configuration first to establish baseline values of boundary layer thickness  $\delta$  and heat transfer coefficient  $h$  to be compared to the missile-fin data. Boundary layers were analyzed using Pitot rakes. To ensure a fully turbulent boundary layer near the fin region, Neumann and Hayes installed a grit strip close to the missile model tip. They noted that the boundary layer remained turbulent over almost the entire surface for all  $\alpha$  because of this grit strip. It remained installed for all tests. In the report, boundary layer profiles are plotted for angles of attack of  $0^\circ$ ,  $-4^\circ$ ,  $-8^\circ$ , and  $-12^\circ$ . The pressure value plotted is the Pitot pressure normalized by the freestream Pitot pressure. Pitot pressure  $P_T$  is the value measured by Pitot probes in high-Mach number flow and it is the stagnation pressure downstream of a normal shock wave. From simulated results,  $P_T$  can be calculated using stagnation pressure, Mach number, and the ratio of specific heats  $\gamma$

along with isentropic flow relations and normal shock wave relations. Algebraically manipulating these relations results in the single expression [10] for Pitot pressure

$$P_T = P_0 \left( \frac{\frac{\gamma+1}{2} M^2}{1 + \frac{\gamma-1}{2} M^2} \right)^{\frac{\gamma}{\gamma-1}} \left( \frac{2\gamma}{\gamma+1} M^2 - \frac{\gamma-1}{\gamma+1} \right)^{-\frac{1}{\gamma-1}} \quad (2.2)$$

where  $P_0$ ,  $M$ , and  $\gamma$  are taken from the point of interest. The non-reacting dry air assumption made for the simulations here results in a constant  $\gamma$  everywhere of 1.4. All baseline boundary layer measurements were taken by Neumann and Hayes at M.S. 107, which is where the fin region began in the missile-fin configuration. The boundary layer thickness  $\delta$  was visually determined by identifying where the knee occurred on the  $P_T$  plots. The knee was where the  $P_T$  profile abruptly changed slope and it was used to define  $\delta$ . For  $\alpha = 0^\circ$ , the measured boundary layer thickness was 1.6 cm. Simulated  $P_T$  boundary layer profiles are compared to experimental profiles in Section 3.3. Also compared are profiles of  $P_T$  in the main shock wave and circumferential distributions of surface pressure at M.S. 107.

Heat transfer coefficients were reported in units of BTU/(ft<sup>2</sup>s<sup>o</sup>R), which are equivalent to

$$\left( 1 \frac{\text{BTU}}{\text{ft}^2 \text{s}^\circ \text{R}} \right) \left( 1.8 \frac{^\circ \text{R}}{\text{K}} \right) \left( \frac{1}{(0.0254 \times 12)^2} \frac{\text{ft}^2}{\text{m}^2} \right) \left( 1055 \frac{\text{J}}{\text{BTU}} \right) = 20440 \frac{\text{W}}{\text{m}^2 \text{K}} \quad (2.3)$$

in SI units. Measured values of  $h$  ranged from 28 W/(m<sup>2</sup>K) for  $\alpha = 0^\circ$  to as high as 92 W/(m<sup>2</sup>K) for  $\alpha = -12^\circ$  on the windward centerline. On the leeward side,  $h$  was measured as low as 3.6 W/(m<sup>2</sup>K) for  $\alpha = -12^\circ$  at  $\phi = 110^\circ$ . These  $h$  measurements were taken at M.S. 89 and were defined using Equation 1.1 with a  $T_{ref}$  of  $0.9T_{0\infty}$ . They are compared to simulated  $h$  values in Section 3.4.

The missile-fin wind tunnel tests were carried out after the baseline tests. An internal mechanical system was installed to vary the length of the cylinder connecting the missile and fin. It connects the fin to the missile model and creates a gap with height  $g_h$ . Data were reported for  $g_h$  values of 0.254 cm, 0.508 cm, 0.762 cm, and 1.016 cm. The angles of attack tested were  $0^\circ$ ,  $-4^\circ$ ,  $-8^\circ$ , and  $-12^\circ$ . A thin-skin insert with thermocouples was installed upstream of the cylinder to measure heating on

the missile surface under the fin. Thermocouples were positioned axially to allow for plots of surface heating distributions along the top centerline on the missile surface.

Neumann and Hayes observed an increase in heating with the fin and cylinder installed. Maximum heat transfer coefficients ranged from 2 to 10 times the baseline level depending on the combination of  $g_h$  and  $\alpha$ . Trends were identified, such as  $h$  generally increasing with  $g_h$ . An exception is that at  $\alpha = -8^\circ$ ,  $h$  was smaller for  $g_h = 1.016$  cm than for  $g_h = 0.508$  cm or  $g_h = 0.762$  cm. Neumann and Hayes inferred that for each  $\alpha$ , there is a specific  $g_h$  where the shock wave boundary layer interaction in the gap changes separation pattern. A drop in  $h$  was theorized to accompany this change. After this drop,  $h$  would continue to rise with increasing  $g_h$ . This phenomenon could not be exactly replicated in the simulations, but separation patterns did change with  $g_h$  and they are discussed in Section 4.2. Finally, an important finding was that maximum  $h$  values always occurred at the closest thermocouple to the cylinder. This thermocouple was located 0.3 cylinder diameters, or 0.476 cm, upstream of the cylinder surface. Neumann and Hayes stated that maximum heat transfer always occurs within the region that is 0.3 cylinder diameter lengths upstream of the cylinder surface. Simulated heat transfer in the gap region is presented and compared to experimental measurements in Chapter 4.

## 2.2 Mesh Generation

Computational fluid dynamics requires a numerical framework to represent the spatial domain. This framework is referred to as a mesh or grid and its purpose is to discretize continuous space into a finite number of points and cells. Software programs with graphical user interfaces are available to aid designers in creating detailed meshes. The commercial program Pointwise [11] was used to create all meshes for the work presented in this thesis.

### 2.2.1 Baseline Configuration

The baseline configuration was meshed first. A CAD program was utilized to draw the 2D contour of the missile model surface, which was then imported into the mesh generation program. Starting with a CAD program allowed for precise dimensioning of the ogive's tip and radius of curvature while enforcing tangency. The tip radius was not disclosed in Neumann and Hayes's technical report, so a relatively sharp value of  $50 \mu\text{m}$  was assumed. Once imported, the contour line served as the base of a 2D grid for the space around the missile model. The total domain was sized to capture the entirety of the main shock wave for all  $\alpha$  and the wake region 43 cm behind the missile model. This 2D grid was then revolved  $180^\circ$  to encompass the 3D space around the model. This revolution results in a symmetry plane that passes through the top and bottom centerlines. The surface grid on the missile model's base, shown in Figure 2.6, was created separately and extruded 43 cm to encompass the wake region. For all grid lines, a hyperbolic tangent spacing function was used to govern point distributions. Point counts of all components vary between coarse, medium, and fine versions of the mesh. Figure 2.3 shows the coarse mesh with component lines labeled and Table 2.2 shows the point counts.

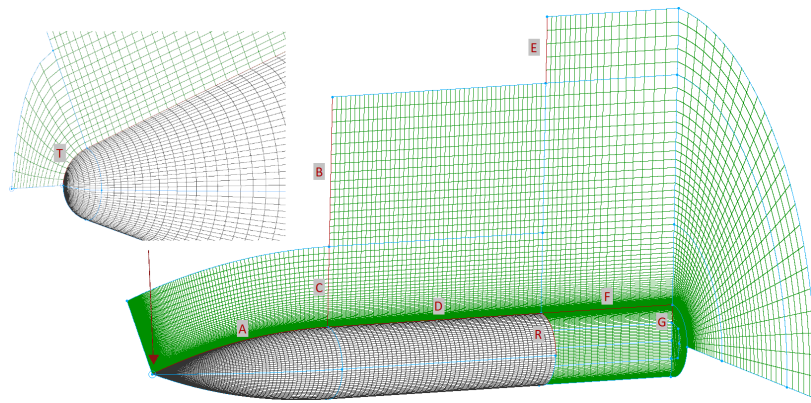


Fig. 2.3. Coarse baseline mesh. Component lines labeled. Some parts hidden for clarity.

Table 2.2.  
Baseline Mesh Point Counts

<b>Component</b>	<b>Coarse</b>	<b>Medium</b>	<b>Fine</b>
A	200	400	800
B	18	25	45
C	100	150	300
D	48	71	141
E	6	7	10
F	20	35	65
G	60	80	140
R	25	45	75
T	9	17	32
$\Delta s$	$8 \times 10^{-6}$ m	$4 \times 10^{-6}$ m	$2 \times 10^{-6}$ m
Total Points	1.4 million	5.6 million	48 million

The first cell wall-normal grid spacing  $\Delta s$  is an important parameter for mesh design. To properly calculate boundary layer effects on wall properties,  $\Delta s$  must be smaller than a certain threshold. This threshold is related to the non-dimensional wall distance coordinate  $y^+$ . For turbulent RANS calculations, a  $\Delta s$  that achieves  $y^+ \leq 1$  is considered sufficient to calculate heat flux. An approximation for a  $\Delta s$  that achieves  $y^+ = 1$  obtained using incompressible turbulent flat plate boundary layer theory [12] is

$$\Delta s = 8.61 Re_{\infty}^{-13/14} \text{ m} \quad (2.4)$$

where  $Re_{\infty}$  is the freestream Reynolds number per unit meter. A derivation of this expression is given in the Appendix. The resulting  $\Delta s$  estimate for this project's  $Re_{\infty}$  is  $2 \times 10^{-6}$  m. From comparison to CFD calculations of achieved  $y^+$ , this approximation underestimates the required  $\Delta s$  for boundary layers not affected by

SWBLI. Results discussed in Chapters 3 and 4 include CFD calculations of achieved  $y^+$ .

### 2.2.2 Missile-Fin Configuration

The fin and cylinder complicate the meshing process. Overall, the missile-fin domain was considered as five different regions: the gap, the space above the fin, the space adjacent to the fin, the missile, and the wake. They were meshed in that order. The missile-fin mesh was created with a structured-block approach, meaning that neighboring regions share grid faces. So, gap meshing was prioritized first to minimize constraints from neighboring regions. As with the baseline mesh, a symmetry plane is employed through the top and bottom centerlines.

The first step was creating a surface mesh on the fin bottom face. Figure 2.4 shows the final design. The region near the fin tip was segmented into a four-sided diamond shape to accommodate a structured grid. Another structured grid wraps around the cylinder and joins with neighboring meshes via two unstructured corner points. The Steger-Sorenson boundary control function [13] was applied to smooth gridlines within and between grids and to ensure orthogonality and specified spacings on grid boundaries. The surface mesh on the bottom fin face was then projected onto the missile surface, creating the first set of 3D structured grid blocks. An important detail is that the cylinder was projected straight down while the rest of the mesh was projected using a closest-point approach. The closest-point approach ensured that gridlines were orthogonal to the missile model surface. The  $\Delta s$  used on the missile model surface for missile-fin meshes was  $5 \times 10^{-6}$  m. Regarding point counts, grids with a larger  $g_h$  generally had more points along the length of the cylinder. No other component of the missile-fin mesh design varied with  $g_h$ . Table 2.3 identifies the cylinder length and total point counts of each mesh.

After generating the grid blocks in the gap, the side and top fin faces were meshed. The regions near the fin tip were segmented into a diamond shape as with the bottom

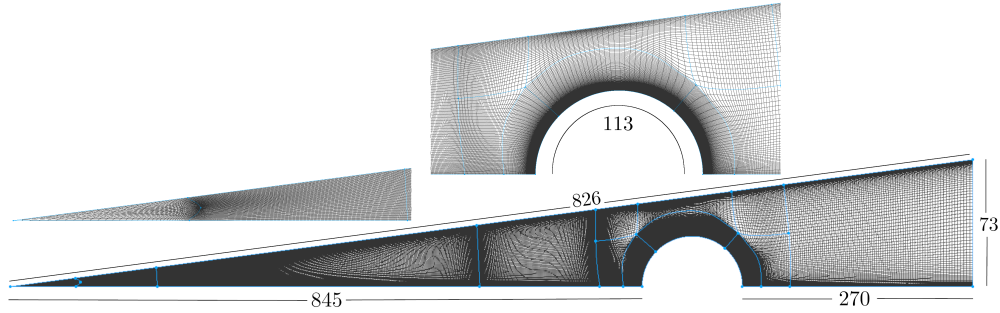


Fig. 2.4. Fin bottom face surface mesh. Point counts labeled.

Table 2.3.  
Missile-Fin Mesh Cylinder and Total Point Counts

$g_h$	Cylinder Points	Total Points
0.508 cm	201	78 million
0.762 cm	201	78 million
1.016 cm	268	91 million
1.270 cm	340	104 million

face. The top face mesh was projected upward to the farfield. The side face mesh was revolved  $180^\circ$ . This revolution required manually created circular lines because the fin face is skewed. Once the spaces above and around the fin were meshed, the missile model grid was created using a similar process as for the baseline configuration mesh. Unlike the baseline mesh, the missile-fin mesh is coarser on the leeward side than the windward side. Last, the space behind the fin was meshed using a translational extrusion. This step involved creating a missile base surface mesh and extruding it 53 cm into the wake region. The total missile-fin mesh, with  $g_h = 0.762$  cm, is shown in Figure 2.5.

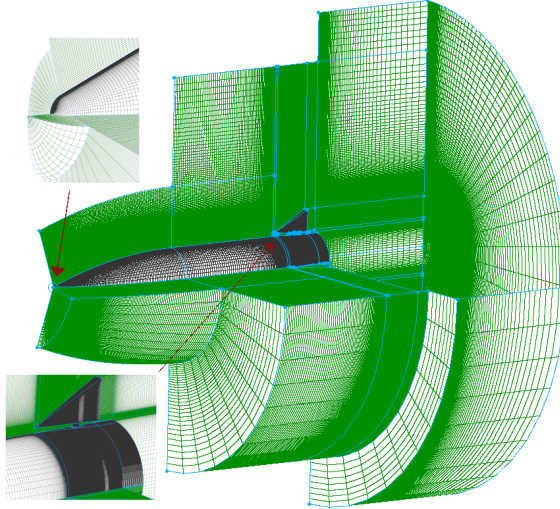


Fig. 2.5. Missile-fin mesh. Some parts hidden for clarity.

### 2.2.3 Classification of Meshes

Classifying meshes depends on the shape of cells and orderability of points. In 2D, a structured grid has only quadrilateral cells and all points can be mapped using  $i, j$  coordinates to a uniform Cartesian lattice. A similar constraint exists in 3D, where structured grids have only hexahedral cells and points can be mapped using  $i, j, k$  coordinates. A grid that does not meet these constraints is unstructured. Mesh classification is important because CFD codes are developed differently for structured grids and unstructured grids. It is easier for computers to work with structured grids because the  $i, j, k$  coordinates efficiently store point connectivity information. However, only simple geometries can be captured using a single structured grid. So, the three main classifications for meshes with complex geometry are overset, structured-block, and fully unstructured.

An overset mesh involves multiple grids overlapping each other and sharing information. The CFD code solves each grid separately, ensuring agreement between solutions in the overlapping regions through appropriate interpolation. If all component grids are structured, then the overall mesh is considered structured. A structured-block mesh is similar to an overset mesh, but there is no overlap. Each component

grid connects to its neighbors via shared lines in 2D and shared faces in 3D. It is generally implied that every grid in a structured-block mesh contains only quadrilateral or hexahedral cells. However, the connectivity between grids can be unstructured. For example, an unstructured corner point joins multiple structured grids in an arrangement that cannot be considered one structured grid. Figure 2.6 shows the coarse missile-base grid for the baseline configuration; one of its two unstructured corner points is identified. Despite their name, structured-block meshes are generally considered unstructured overall and most CFD codes treat them as fully unstructured. A fully unstructured mesh has no requirement on cell shape.

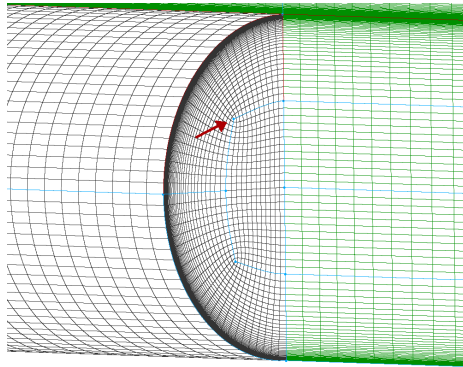


Fig. 2.6. Coarse missile-base grid for baseline configuration. One of two unstructured corner points identified with arrow.

All meshes created for this thesis are structured-block. This approach was chosen based on familiarity. Other approaches are viable and a skilled designer could grid the baseline and missile-fin domains using a fully unstructured or overset mesh. Even though structured grids are preferred on surfaces and around shock waves, fully unstructured meshes can take a hybrid approach and use hexahedral cells in certain regions and tetrahedral cells elsewhere [14].

### 2.3 Simulation Configuration

The DoD software package Kestrel was utilized for all presented simulations. Kestrel [15] is a package of CFD solvers and tools that includes capabilities for prescribed body motion, propulsion, and multi-physics modeling. The specific tool used for this thesis, KCFD, is a finite-volume, unstructured, cell-centered solver. It has multiple options for many aspects of the numerical schemes involved with simulation. The version of Kestrel used for almost all simulations was 10.2rc4. The exception is that for simulations where  $g_h = 0.508$  cm, version 10.3rc5 was used. This later version of Kestrel calculated better results for cases where  $g_h = 0.508$  cm than the older version with identical simulation configuration settings. Table 2.4 lists some of the simulation configuration settings used for the simulations presented in this thesis. In addition to these settings, the freestream flow conditions and desired angles of attack were inputs in Kestrel. The timestep was calculated as a function of model length and freestream velocity using a relation recommended by Kestrel developers for steady-state solutions. Since steady-state solutions were desired, experimentation was done with local time stepping, but that method was found to take more iterations to converge. The highest order available, second order, was used for the spatial, temporal, and turbulence spatial accuracies. The wall condition was selected to best simulate the short-duration wind tunnel tests with the model injected near room temperature. The method used to calculate convective flux Jacobians was van Leer's [16], which was recommended by Kestrel developers for perfect gasses. They also recommended their own limiter Kestrel+. It is based on the Barth/Jespersen scheme [17] with an added shock sensor. For SWBLI, developers recommended the Spalart-Allmaras (SA) [18] turbulence model for steady, attached flows. Wall functions were enabled but KCFD only activated them on surfaces where  $\Delta s$  achieved  $y^+ \geq 3$ . This threshold was not reached on the relevant parts of the missile surface. The intent was for wall functions to activate on fin surfaces where  $\Delta s$  may be too large to achieve  $y^+ < 3$ . The HLLE++ [19] inviscid flux scheme was used for its

numerous beneficial features including reduced susceptibility to carbuncles and good performance regardless of grid-alignment with shock waves. The viscous flux scheme, LDD+, was chosen rather than the other, low order, option. An advective temporal damping parameter of 0.1 was also used. KCFD utilized a Gauss-Seidel iterative method to solve linear equations and a relaxation factor of 0.9 was applied in that method.

Table 2.4.  
Simulation Settings

Equations Solved	Reynolds-averaged Navier Stokes
Fluid	Air Perfect Gas
Turbulence Model	SA (one-equation)
Spatial Accuracy	Second Order
Temporal Accuracy	Second Order
Time Stepping	Global
Time Step	0.0001 seconds
Turbulence Spatial Accuracy	Second Order
Wall Condition	Isothermal, 300 K
Wall Functions	Yes
Limiter	Kestrel+
Convective Flux Jacobian	Van Leer
Inviscid Flux	HLLE++
Viscous Flux	LDD+

## 2.4 Computational Resources

The simulations for this thesis were executed on the ARL high performance cluster Excalibur. Its standard memory nodes each contain two 16-core Intel Xeon E5

processors sharing 128 GB of memory [20]. Accessing Excalibur involves using a secure online portal or SSH client to interact with its Linux environment. Computational jobs are submitted via a PBS system that tracks usage of allocated hours and available queues.

The average time per iteration for the simulations ranged from 0.064 seconds for the coarse baseline mesh to 1.9 seconds for the missile-fin meshes. The baseline simulations used varying node numbers, with the coarse, medium, and fine-grid simulations each using 27, 35, and 50 nodes, respectively. Many more nodes were used for the missile-fin simulations. The total number of nodes used for every missile-fin simulation where  $g_h > 0.508$  cm was 137. This number was calculated based on a recommendation of 20,000 gridpoints per core from a computational scaling study performed using 3D grids with a different unstructured CFD solver [21]. The simulations where  $g_h = 0.508$  cm used 90 nodes on the ERDC cluster Onyx.

Excalibur has a large-storage directory available for holding output files from submitted jobs. As Kestrel runs, it outputs visualization files at specified increments that contain the entire solution. If Tecplot [22] is designated as the post-processing tool, the visualization files will have extension .plt and be easily analyzable. They contain all solution information grouped into zones designated by specified mesh surfaces. The solution information for the volume of space between surfaces is also contained in its own zone. For this project, the sizes of the missile-fin grids ranged from 4 GB to 6 GB. The visualization files ranged in size from 9 GB to 13 GB.

## 2.5 Parametric Study Overview

The parameters varied for the baseline simulations were mesh refinement and angle of attack. Table 2.5 summarizes the cases in the parametric study. For the missile-fin simulations, the parameters varied were gap height and angle of attack. The four angles of attack simulated throughout the parametric study were  $0^\circ$ ,  $-4^\circ$ ,  $-8^\circ$ , and  $-12^\circ$ . The four gap heights simulated were 0.508 cm, 0.762 cm, 1.016 cm, and

1.270 cm. Neumann and Hayes reported measurements for gap heights of 0.254 cm, 0.508 cm, 0.762 cm, and 1.016 cm, but simulations for  $g_h = 0.254$  cm could not be properly executed. So, the  $g_h = 1.270$  cm simulation was added in its place.

Table 2.5.  
Parametric Study Outline

<b>Case</b>	<b>Angles of Attack</b>
Baseline - Coarse	$0^\circ, -4^\circ, -8^\circ, -12^\circ$
Baseline - Medium	$0^\circ, -4^\circ, -8^\circ, -12^\circ$
Baseline - Fine	$0^\circ, -4^\circ, -8^\circ, -12^\circ$
Missile-Fin - $g_h = 0.508$ cm	$0^\circ, -4^\circ, -8^\circ, -12^\circ$
Missile-Fin - $g_h = 0.762$ cm	$0^\circ, -4^\circ, -8^\circ, -12^\circ$
Missile-Fin - $g_h = 1.016$ cm	$0^\circ, -4^\circ, -8^\circ, -12^\circ$
Missile-Fin - $g_h = 1.270$ cm	$0^\circ, -4^\circ, -8^\circ, -12^\circ$

### 3. BASELINE RESULTS

The baseline configuration involves the plain missile model absent of a fin or cylinder. Properties of the baseline configuration establish levels that can be compared to properties of the missile-fin configuration. Simulations of the baseline configuration were designed to calculate results comparable to wind tunnel test data gathered by Neumann and Hayes [8]. The simulated freestream flow conditions, dimensions of the missile model, and angles of attack matched those used in the tests. Plots of simulated properties include experimental data wherever possible. The first results shown here are used to establish solution convergence at the final simulation iteration. Then, properties are analyzed in a grid resolution study that involves a coarse, medium, and fine mesh of the baseline configuration. After these sections about convergence and grid resolution, only results from the final iteration and fine mesh are used in figures unless otherwise noted. The overall flow structure is analyzed in a section that includes plots of Mach number, skin friction coefficient, and surface pressure. Last, heat transfer calculations are compared to experimental measurements.

#### 3.1 Solution Convergence

Every baseline simulation involved 75,000 total iterations. Intermediate solutions were saved at iterations 25,000 and 50,000 to be compared to the final result. For all properties analyzed, the intermediate solutions are virtually identical to each other and the final result. The analyzed properties from iterations 25,000, 50,000 and 75,000 differ by less than 0.01%. This agreement implies that a steady state solution was achieved after 25,000 iterations that is independent of additional iterations. Plots of surface pressure, streamwise skin friction coefficient  $C_{fx}$ , and heat flux  $\dot{q}$  along the top centerline are presented in Figures 3.2 through 3.4 to demonstrate convergence.

At the scale used in these figures, the lines corresponding with each iteration overlap and cannot be distinguished. The lines still appear identical even at much smaller scales.

Results used to establish convergence follow expected trends. Larger angles of attack are associated with greater levels of surface pressure, skin friction, and heat flux on the windward side. Distributions flatten near M.S. 57, which is where the ogive section of the missile model ends. This change in surface geometry would be expected to alter the development of the boundary layer and the gradient of fluid properties near the wall. Also, the Reynolds analogy theorizes that turbulent momentum flux and heat flux are closely related phenomena [23]. It can be used to state that skin friction and heat flux are proportional to each other in certain turbulent boundary layers, so it is not surprising that plots of those properties shown here have similar shapes.

### 3.2 Grid Resolution Study

Simulations of the baseline configuration involved three mesh resolutions. By total point count, the medium mesh is 4 times larger than the coarse mesh, and the fine mesh is 8.5 times larger than the medium mesh. In terms of the first cell normal grid spacing off of the missile model surface, the medium mesh  $\Delta s$  is half of the coarse mesh  $\Delta s$ , and the fine mesh  $\Delta s$  is half of the medium mesh  $\Delta s$ . Figures 3.5 and 3.6 plot distributions of achieved  $y^+$  on the top centerline for every  $\alpha$  and mesh resolution. Every mesh resolution achieved  $y^+ < 1$  almost everywhere on the top centerline for every  $\alpha$ .

A grid independent solution should have equivalent values, within an error, for properties of interest between levels of mesh refinement. The same properties used to establish solution convergence were used to study grid independence. Figures 3.7 through 3.9 compare simulated distributions of each property along the top centerline for every  $\alpha$  and mesh resolution. Values for the flat section of the missile model are

enlarged on the right-hand side in each figure. All properties slightly increase in value as mesh resolution increases. For the  $\alpha = -12^\circ$  case, the variances between the medium and fine results for surface pressure,  $C_{fx}$ , and  $\dot{q}$  on the flat part of the missile model are less than 2%. These differences are small enough to suggest that additional refinement would not significantly affect results.

### 3.3 Overall Flow Structure

The set of figures for this section begins with a series of Mach-contour plots for every angle of attack to illustrate large-scale flow features. They are shown in Figures 3.10 through 3.13, and they were generated from the fine-mesh simulations. As  $\alpha$  increases, the bow shock wave on the windward side increase in strength while the boundary layer on the windward side decreases in thickness. The leeward side involves a shock wave and an expansion region where flow speed approaches Mach 7. The wake region changes shape with  $\alpha$ .

Surface pressure measurements were taken by Neumann and Hayes along the circumference of the missile model at M.S. 107. Comparable data plotted in the technical report are for  $\alpha = -4^\circ$  and  $\alpha = -8^\circ$ . Figure 3.14 plots the simulated surface pressure distributions compared to experimental distributions. Simulated surface pressure distributions agree extremely well with measured distributions on the windward side of the missile model. On the leeward side, the  $\alpha = -4^\circ$  simulated distribution agrees very well with measurements, while the  $\alpha = -8^\circ$  simulated distribution deviates from measurements near  $\phi = 135^\circ$ . The complex flow separation and reattachment on the leeward side was likely not accurately simulated. Tailoring of the mesh may be necessary to accurately calculate surface properties on the leeward side for larger angles of attack [24].

Boundary layers were investigated in the wind tunnel tests using Pitot rakes. A row of closely-spaced Pitot tubes were placed near the missile model surface on the top centerline at M.S. 107. The tubes measured Pitot pressure  $P_T$ , which is the

stagnation pressure downstream of a normal shock wave. In the technical report, Neumann and Hayes plotted  $P_T$  normalized by the freestream Pitot pressure  $P_{T\infty}$ . As discussed in Chapter 2.1,  $P_T$  can be calculated using simulated values of  $P_0$ ,  $M$ , and  $\gamma$ . The calculated value of  $P_{T\infty}$  for this project is 52900 Pa. Figures 3.15 and 3.16 plot the simulated boundary layer Pitot pressure profiles compared to experimental data points. Visually determined experimental  $\delta$  locations are also displayed. For every angle of attack, the simulated boundary layer thickness  $\delta$  agrees very well with the experimentally determined thickness. Neumann and Hayes determined  $\delta$  values by visually selecting knee locations on their  $P_T$  plots. For  $\alpha = 0^\circ$  and  $\alpha = -4^\circ$ ,  $\delta$  coincided with a level directly above one of the Pitot probe measurements. For  $\alpha = -8^\circ$  and  $\alpha = -12^\circ$ ,  $\delta$  fell between two Pitot probe measurements. Every simulated knee location falls between the two Pitot probe measurements above and below the experimentally determined  $\delta$ . The overall simulated boundary layer profile for  $\alpha = -12^\circ$  agrees extremely well with data and the overall simulated boundary layer profile for  $\alpha = -8^\circ$  agrees very well with data. For  $\alpha = -4^\circ$ , an experimentally observed curved profile shape above the knee location is not simulated. This discrepancy is also present for  $\alpha = 0^\circ$ , but to a lesser extent. There is also some discrepancy below the knee location for  $\alpha = 0^\circ$ . Figure 3.17 plots  $\delta$  as a function of  $\alpha$  on the top centerline at M.S. 107. Boundary layer thickness decreases with increasing  $\alpha$  for the angles of attack studied. A second-order polynomial fits the simulated  $\delta$  values as a function of  $\alpha$ . Experimental  $\delta$  values are also shown. Both experimental and simulated  $\delta$  values were determined visually.

A large Pitot rake was used by Neumann and Hayes to probe the main shock wave over the missile model at M.S. 107. Comparable data plotted in the technical report are for  $\alpha = -4^\circ$  and  $\alpha = -8^\circ$ . Figure 3.18 plots the simulated shock wave Pitot pressure profiles compared to experimental data points. Simulated shock wave profiles agree very well with Pitot probe measurements. There is a second knee between the edge of the boundary layer and the front of the main shock wave, and simulated locations of that knee match experimental locations. However, the lower boundary of

the main shock wave front, where a nearly discontinuous change in  $P_T$  occurs, differs between simulated results and wind tunnel measurements. The simulations predict that the location of the main shock wave front is below the placement of the highest Pitot probes. The highest Pitot probes did not measure the nearly discontinuous change in  $P_T$ . Simulated locations of the lower boundary of the main shock wave front approach agreement with measurements as mesh resolution increases. Improving the alignment of the mesh with the shock wave, or using an extremely fine mesh, would likely remove this discrepancy.

### 3.4 Heat Transfer

Heat transfer coefficients were measured by Neumann and Hayes along the circumference of the missile model at M.S. 89. Each of their plots contains a cluster of many data points spanning the range of  $\phi$ . To facilitate comparison to simulated  $h$  distributions, the upper and lower boundaries of their clusters are displayed in the figures here. Figures 3.19 and 3.20 plot the simulated  $h$  distributions along the circumference of the missile model at M.S. 89. All simulated  $h$  values are defined using Equation 1.1 with a reference temperature of  $0.9T_{0\infty}$ . Similar to the plot of surface pressure in Figure 3.14, simulated  $h$  distributions agree very well with experimental distributions on the windward side of the missile model. Simulated  $h$  distributions when  $\alpha = 0^\circ$  and  $\alpha = -4^\circ$  fall within the data point clusters near their lower boundaries. Simulated  $h$  distributions when  $\alpha = -8^\circ$  and  $\alpha = -12^\circ$  fall near the center of the clusters on the windward side. On the leeward side, the simulations do not capture the shape of the  $h$  distributions measured in experiments near  $\phi = 135^\circ$ . The phenomena causing these discrepancies are likely related to the phenomena causing the discrepancy in surface pressure. It is possible that an alternative turbulence model may calculate surface properties on the leeward side more accurately. Flow on the leeward side of the missile model was noted by Neumann and Hayes to be complex due to flow separation and reattachment. Fortunately, heat transfer and surface pressure are lower

on the leeward side, so the maximum levels of those properties are being accurately predicted by the simulations.

For every angle of attack, the maximum value of  $h$  at M.S. 89 occurs on the top centerline of the missile model. Figure 3.21 plots  $h$  as a function of  $\alpha$  on the top centerline at M.S. 89. Ranges of experimental measurements are included. Values of  $h$  on the top centerline increase with increasing  $\alpha$  for the angles of attack studied. A second-order polynomial fits the simulated  $h$  values as a function of  $\alpha$ .

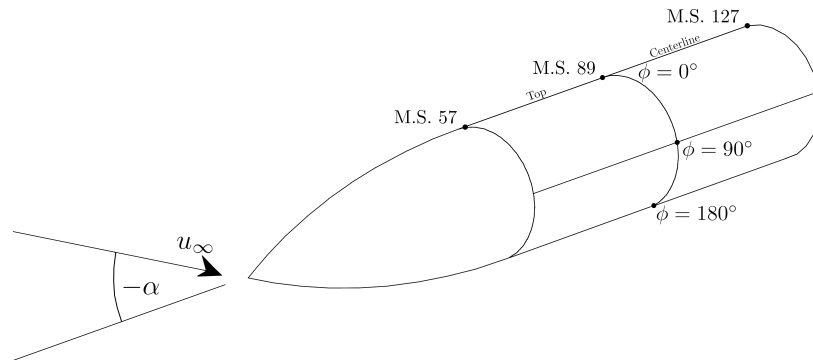


Fig. 3.1. Missile model coordinate system.

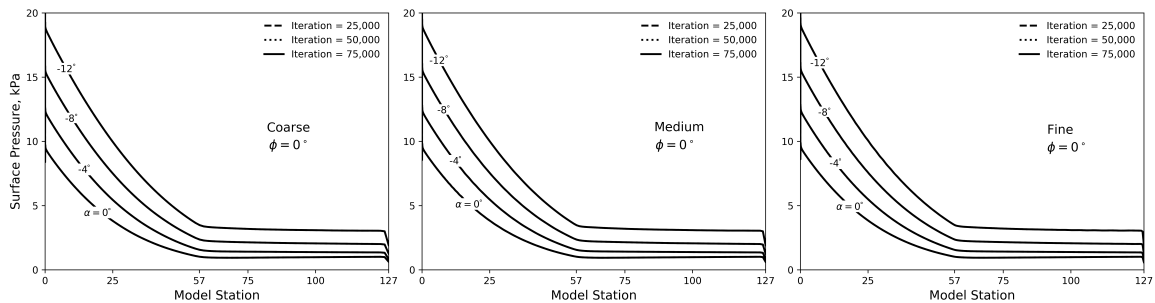


Fig. 3.2. Surface pressure on top centerline. Separate plots for each mesh resolution.

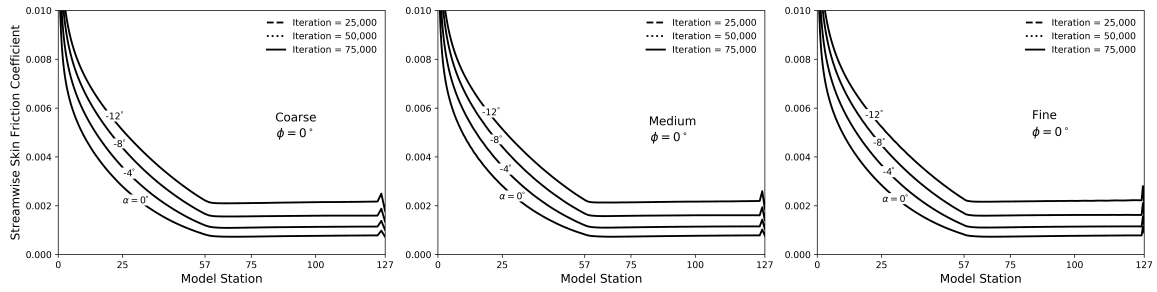


Fig. 3.3. Streamwise skin friction coefficient on top centerline. Separate plots for each mesh resolution.

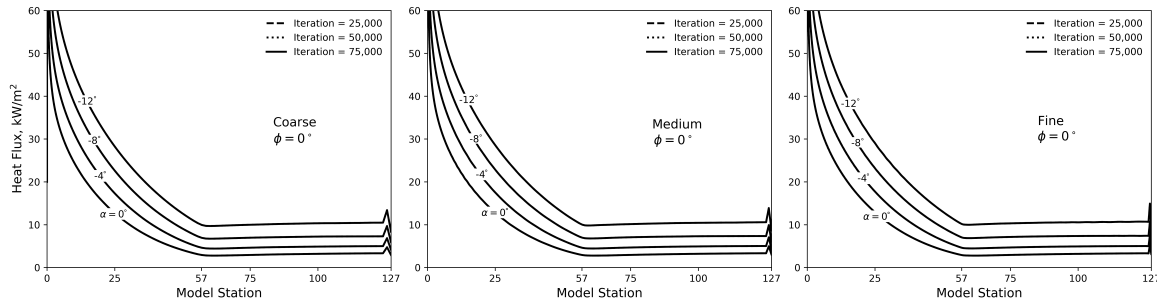


Fig. 3.4. Heat flux on top centerline. Separate plots for each mesh resolution.

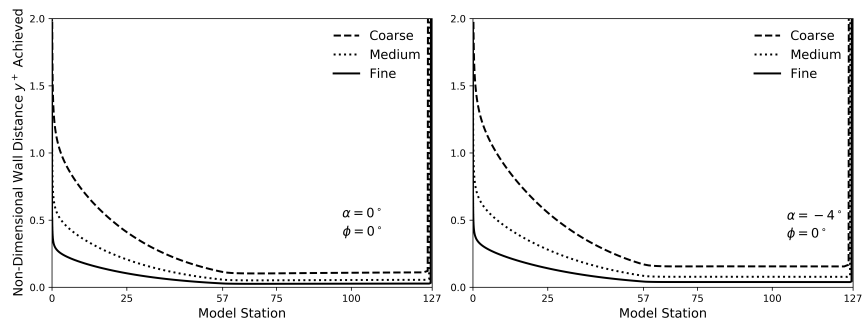


Fig. 3.5. Achieved  $y^+$  on top centerline for angles of attack of  $0^\circ$  and  $-4^\circ$ .

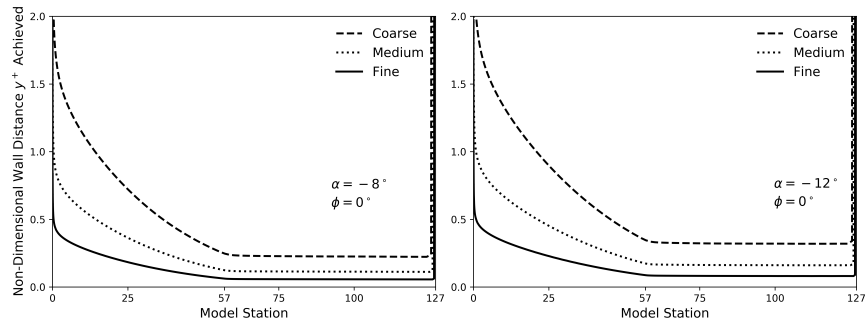


Fig. 3.6. Achieved  $y^+$  on top centerline for angles of attack of  $-8^\circ$  and  $-12^\circ$ .

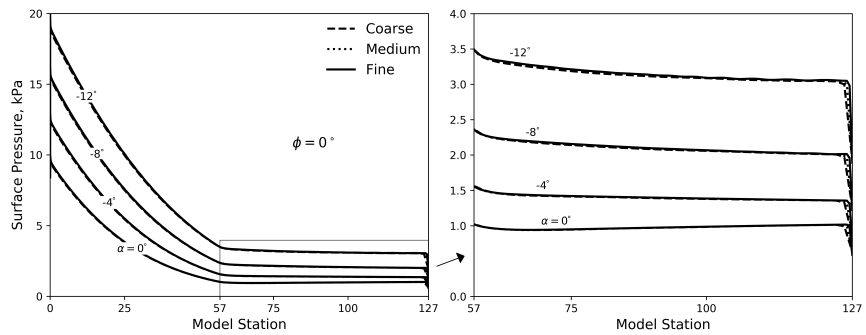


Fig. 3.7. Surface pressure on top centerline. Flat section of missile model enlarged on right-hand side.

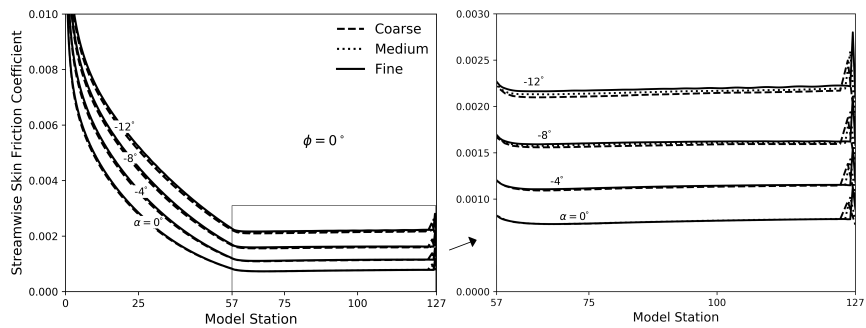


Fig. 3.8. Streamwise skin friction coefficient on top centerline. Flat section of missile model enlarged on right-hand side.

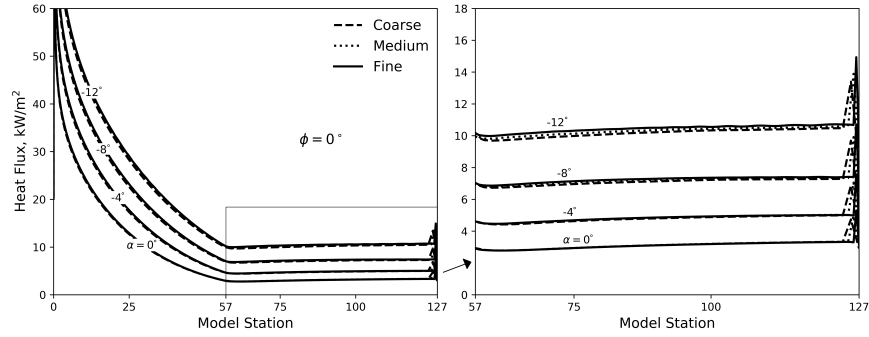


Fig. 3.9. Heat flux on top centerline. Flat section of missile model enlarged on right-hand side.

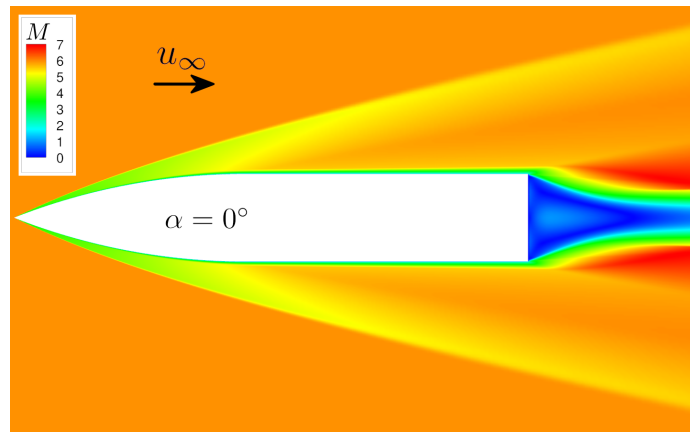


Fig. 3.10. Mach-contour plot of baseline simulation for  $\alpha = 0^\circ$ . Centerplane slice from 3D simulation.

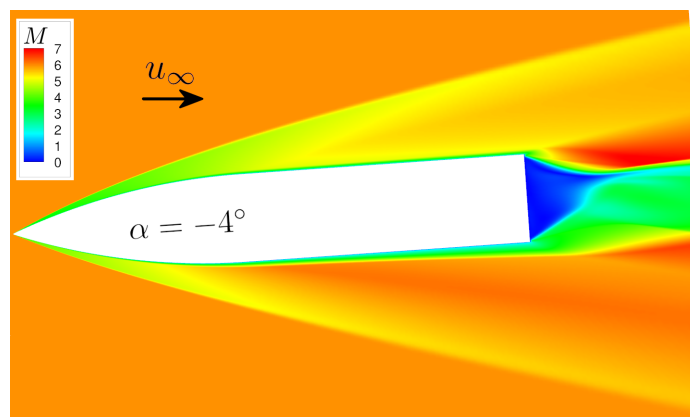


Fig. 3.11. Mach-contour plot of baseline simulation for  $\alpha = -4^\circ$ . Centerplane slice from 3D simulation.

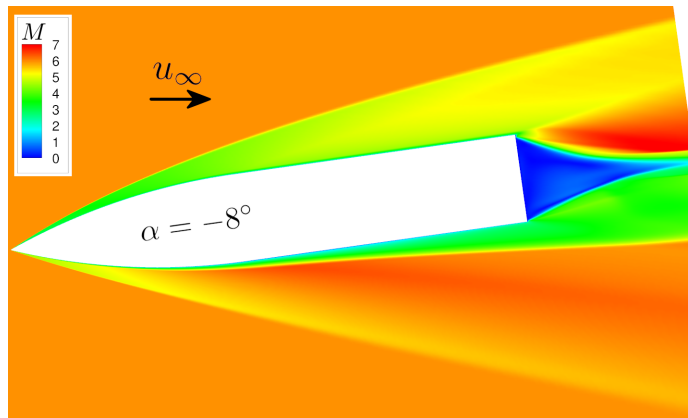


Fig. 3.12. Mach-contour plot of baseline simulation for  $\alpha = -8^\circ$ . Centerplane slice from 3D simulation.

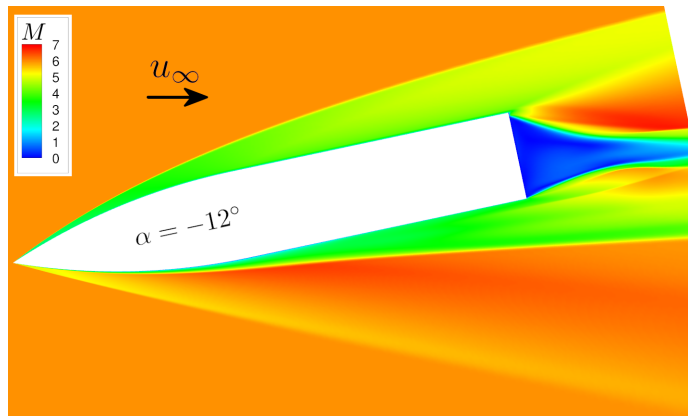


Fig. 3.13. Mach-contour plot of baseline simulation for  $\alpha = -12^\circ$ . Centerplane slice from 3D simulation.

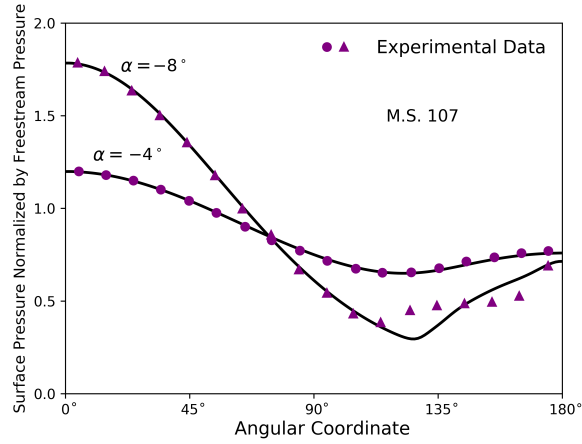


Fig. 3.14. Surface pressure divided by  $P_\infty$  along the missile model circumference at M.S. 107. Black lines are simulated distributions.

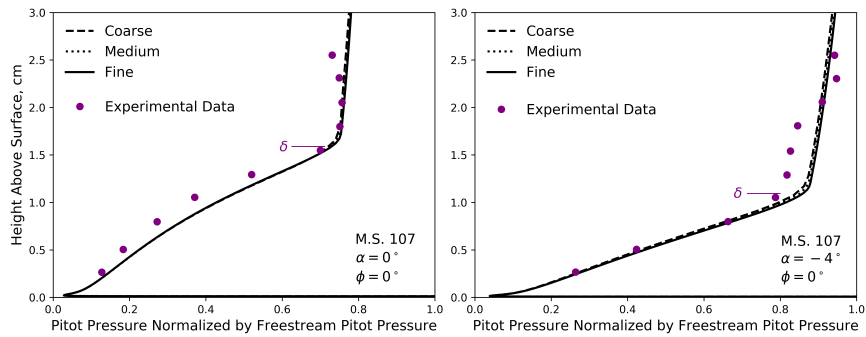


Fig. 3.15. Boundary layer  $P_T/P_{T\infty}$  profile at M.S. 107 for angles of attack of  $0^\circ$  and  $-4^\circ$ . Black lines are simulated distributions.

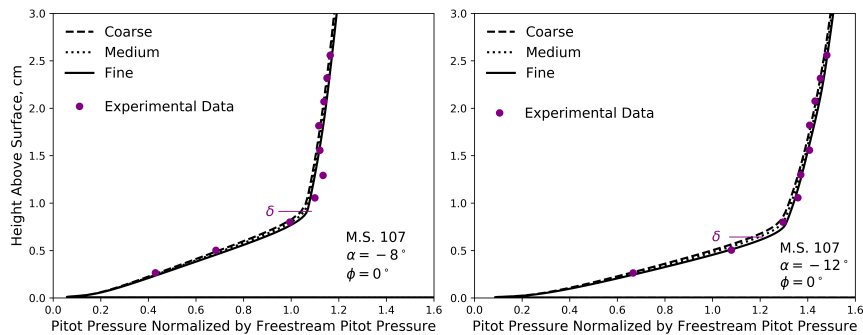


Fig. 3.16. Boundary layer  $P_T/P_{T\infty}$  profile at M.S. 107 for angles of attack of  $-8^\circ$  and  $-12^\circ$ . Black lines are simulated distributions.

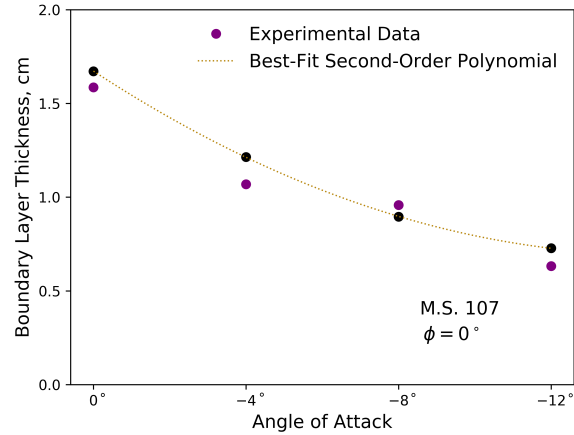


Fig. 3.17. Boundary layer thickness on top centerline at M.S. 107 as function of  $\alpha$ . Black markers are simulated values.

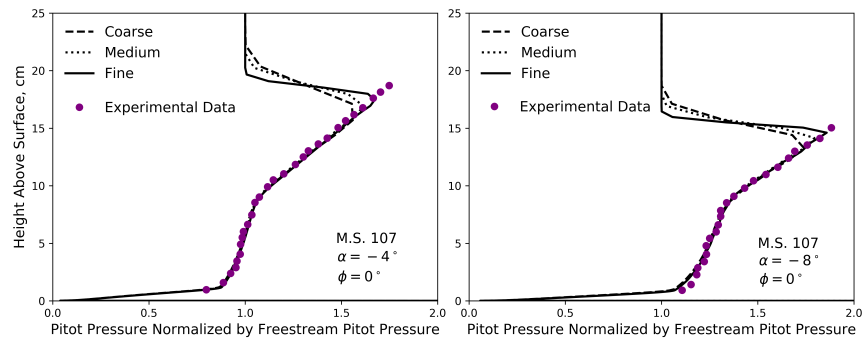


Fig. 3.18. Shock wave  $P_T/P_{T\infty}$  profiles at M.S. 107 for angles of attack of  $-4^\circ$  and  $-8^\circ$ . Black lines are simulated distributions.

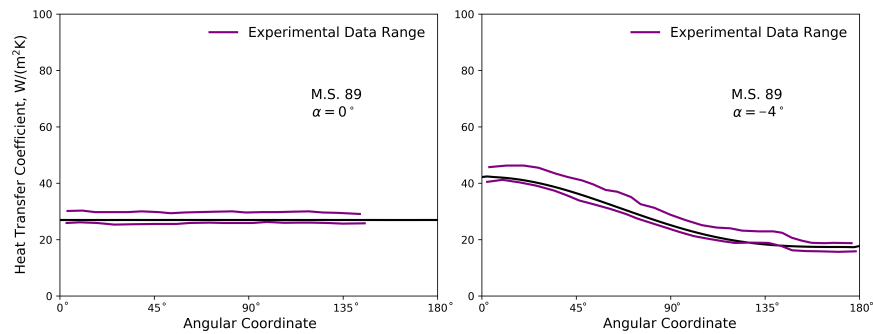


Fig. 3.19. Heat transfer coefficient along circumference of missile model at M.S. 89 for angles of attack of  $0^\circ$  and  $-4^\circ$ . Black lines are simulated distributions.

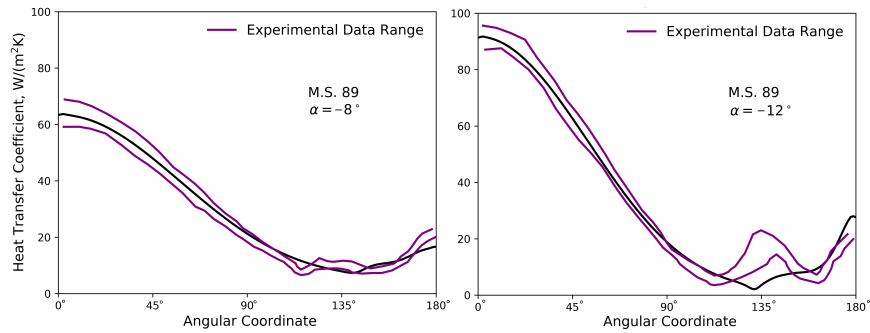


Fig. 3.20. Heat transfer coefficient along circumference of missile model at M.S. 89 for angles of attack of  $-8^\circ$  and  $-12^\circ$ . Black lines are simulated distributions.

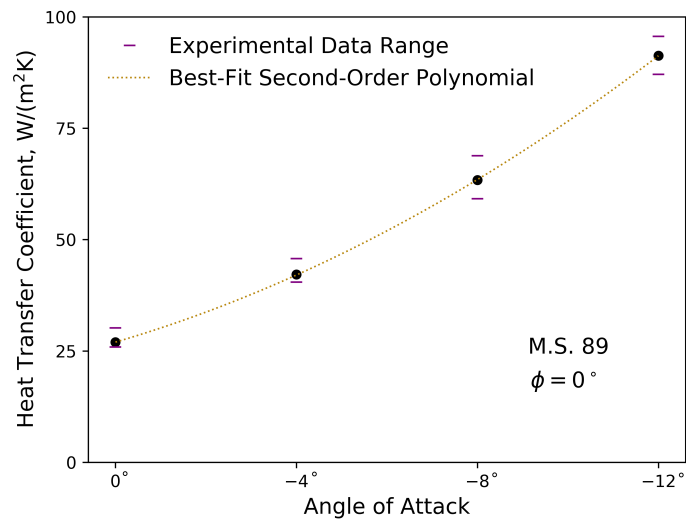


Fig. 3.21. Heat transfer coefficient at M.S. 89 on top centerline as function of  $\alpha$ . Black markers are simulated values.

## 4. MISSILE-FIN RESULTS

The missile-fin configuration involves the same missile model as the baseline configuration, but with an added fin and connecting cylinder. The diameter of the cylinder and the dimensions of the fin remained constant throughout Neumann and Hayes's wind tunnel tests and throughout the simulations. The gap height between the fin and missile was varied in a parametric study to investigate its effects on heating in the gap region. The first results shown here were used to establish solution convergence at the final simulation iteration. After this section, only solutions from the final iteration are shown unless otherwise noted. Then, the overall flow structure is presented with plots of Mach number, skin friction coefficient, and surface pressure. Discussion focuses on variations between cases in the parametric study. Last, heat transfer calculations are compared to experimental measurements and analyzed in terms of their increase over the baseline levels.

### 4.1 Solution Convergence

All missile-fin simulations were carried out for at least 75,000 iterations. For most simulations, calculated properties at iterations 50,000 and 75,000 were confirmed to vary by less than 0.05% in relevant regions. The main exception is the simulation for  $g_h = 1.270$  cm and  $\alpha = 0^\circ$ . For that simulation, the calculated properties in the gap region at iterations 25,000, 50,000, and 75,000 do not agree with each other. Convergence was still not achieved after many more iterations. Results from the solution at iteration 75,000 are presented here. For the simulations where  $g_h = 0.508$  cm, 100,000 total iterations were carried out and calculated properties at iterations 75,000 and 100,000 were confirmed to vary by less than 0.05%. This exception is not related to convergence issues, but rather differently designated iteration checkpoints.

The main region of interest on the missile-fin configuration is the top centerline upstream of the cylinder in the gap region. All distributions plotted in this chapter are along that line. Figure 4.1 illustrates the top centerline in the gap region and identifies the distance coordinate utilized on plots. This coordinate, with symbol  $X/D$ , represents the distance upstream of the cylinder surface as a multiple of cylinder diameter lengths. The gap region extends upstream to the fin tip, where  $X/D = 6.3$ .

The properties analyzed to confirm solution convergence were surface pressure, streamwise skin friction coefficient  $C_{fx}$ , and heat flux  $\dot{q}$ . Figures 4.2 through 4.7 plot the distributions of these properties along the top centerline in the gap region. For surface pressure and  $\dot{q}$  distributions, values are plotted on a logarithmic scale. Surface pressure distributions remain at the baseline level until  $X/D = 6$ . Then, they increase gradually until  $X/D = 2$ , where they rise sharply. The gradual increase near  $X/D = 6$  begins further downstream for larger gap heights. The distribution for the case where  $g_h = 1.016$  cm and  $\alpha = -4^\circ$  has a noticeably different shape than those of the other cases. Locations of maximum surface pressure are always downstream of  $X/D = 0.3$ . These maximum surface pressure calculations are between 40 kPa and 60 kPa for  $g_h > 0.508$  cm, and about 30 kPa for  $g_h = 0.508$  cm. For every gap height, maximum surface pressure occurs when  $\alpha = -12^\circ$ . Streamwise skin friction coefficient distributions generally become negative slightly downstream of  $X/D = 2$  for  $g_h < 1.270$  cm. The points where  $C_{fx} = 0$  indicate boundary layer separation or reattachment. The case where  $g_h = 1.016$  cm and  $\alpha = -4^\circ$  involves separation closer to the cylinder than any other case. Reattachment occurs downstream of  $X/D = 0.3$  in all cases. Shapes of the heat flux distributions are similar to those of the surface pressure distributions. One difference is that near  $X/D = 6$ ,  $\dot{q}$  distributions oscillate as if a physical disturbance was present. This irregularity is likely caused by poor-quality grid cells near the tip of the fin bottom surface mesh. Figure 2.4 shows the diamond-shaped section of the mesh near the fin tip, which was needed to ensure structured grids. Many skewed cells exist in this region, which likely caused the irregularities in the  $\dot{q}$  distributions. Given that the distributions are close to baseline

levels near  $X/D = 6$ , it is assumed that these disturbances do not affect results closer to the cylinder. Also, simulated missile-fin  $\dot{q}$  values on the top centerline at M.S. 89 were confirmed to vary by less than 1% with the simulated baseline  $\dot{q}$  values at that same location.

## 4.2 Overall Flow Structure

A set of Mach-contour plots were generated to illustrate flow features around the fin region. They are presented in Figures 4.8 through 4.11. All plots are centerplane slices from the  $g_h = 0.762$  cm simulations. As  $\alpha$  increases, the boundary layer upstream of the fin decreases in thickness. There is an oblique shock wave above the top surface of the fin that decreases in downstream Mach number with increasing  $\alpha$ . The wake region behind the fin does not appear to vary much with  $\alpha$ . In the gap region, the boundary layer remains attached until about 2 cylinder diameter lengths upstream of the cylinder surface. There, a SWBLI occurs involving separation of the missile boundary layer, separation of the boundary layer on the fin bottom surface, and at least two recirculation bubbles. Figure 4.12 utilizes streamlines to illustrate the SWBLI in the gap region for the case where  $g_h = 0.762$  cm and  $\alpha = 0^\circ$ . The extent of the larger recirculation bubble corresponds with the negative section of the  $C_{fx}$  distribution shown in Figure 4.4. Maximum values of surface pressure and  $\dot{q}$ , which occur very close to the cylinder, appear to correspond with the points of reattachment of the larger recirculation bubble.

Surface pressure distributions are plotted in Figures 4.13 and 4.14. They are normalized by the surface pressure values on the top centerline at M.S. 107 from the fine-mesh baseline simulations. There is one baseline level for each  $\alpha$ . Maximum values of surface pressure occur closer to the cylinder than  $X/D = 0.3$ . For almost every case, surface pressure is below 5 times the baseline level upstream of  $X/D = 0.5$ . Downstream of  $X/D = 0.3$ , the surface pressure distribution peaks at 23 times the

baseline level for the case where  $g_h = 1.270$  cm and  $\alpha = -4^\circ$ . For every  $\alpha$ , maximum levels of surface pressure rise with increasing  $g_h$ .

Streamwise skin friction coefficient distributions are plotted in Figures 4.15 through 4.18. On the right-hand side in every figure, the section of the distribution downstream of  $X/D = 0.3$  is enlarged. The distributions generally become negative near  $X/D = 1.5$ . For  $\alpha = -4^\circ$ , the distributions for  $g_h = 1.016$  cm and  $g_h = 1.270$  cm become negative significantly more downstream than those for the smaller gap heights. For the cases where  $\alpha = -8^\circ$  and  $\alpha = -12^\circ$ , the trend in separation location reverses for the largest gap height. Very close to the cylinder,  $C_{fx}$  distributions do return to positive values. Except for the case where  $g_h = 0.508$  cm and  $\alpha = 0^\circ$ , the points where the  $C_{fx}$  distributions return to positive values nearly coincide with the locations of maximum heat transfer. The locations of maximum heat transfer are indicated with markers on the right-hand side in every figure.

Distributions of the achieved  $y^+$  are plotted in Figures 4.19 and 4.20. For the  $\Delta s$  of  $5 \times 10^{-6}$  m used on the missile surface,  $y^+ < 2$  is achieved everywhere in the gap region in every case. This criterion is also satisfied on the entire cylinder surface in every case. The  $\Delta s$  used on the cylinder surface was  $2.5 \times 10^{-6}$  m.

### 4.3 Heat Transfer

Neumann and Hayes reported  $h$  distributions along the top centerline in the gap region for  $g_h = 0.762$  cm for every  $\alpha$ . By utilizing the maximum levels in Figure 6.11 of their technical report, these distributions were normalized by their baseline levels. Most  $h$  measurements were taken upstream of  $X/D = 2$ , where they were close to the baseline levels. Going downstream from  $X/D = 2$ , measured  $h$  distributions increased, then decreased, then increased sharply at the closest measurement to the cylinder. The closest measurements to the cylinder were taken at  $X/D = 0.3$ , and they were the maximum  $h$  measurements for every  $\alpha$ .

Simulated  $h$  distributions for  $g_h = 0.762$  cm are plotted and compared to experimental distributions in Figures 4.21 and 4.22. They are normalized by the  $h$  values on the top centerline at M.S. 107 from the fine-mesh baseline simulations. These baseline levels are 28.1 W/(m<sup>2</sup>K), 43.2 W/(m<sup>2</sup>K), 64.1 W/(m<sup>2</sup>K), and 92.1 W/(m<sup>2</sup>K) for angles of attack of 0°, -4°, -8°, and -12°, respectively. All simulated  $h$  values are defined using Equation 1.1 with a reference temperature of  $0.9T_{0\infty}$ . Upstream of  $X/D = 2$ , simulated  $h$  distributions agree well with experimental distributions. Simulated distributions begin to rise slightly downstream of  $X/D = 2$ , which is also where measured  $h$  distributions began to rise. Simulated distributions do increase and decrease going downstream from  $X/D = 2$ , but they do not follow the same shape as experimental distributions. At  $X/D = 0.3$ , all simulated  $h$  levels are below measured  $h$  levels. However, simulated  $h$  distributions reach maximum levels, very close to the cylinder, that are much higher than the measured levels at  $X/D = 0.3$ . These simulated maximum levels occur closer to the cylinder than  $X/D = 0.1$ . They are 20 to 25 times the baseline level.

Plots of the simulated  $h$  distributions for every case are presented in Figures 4.23 and 4.24. The simulations for  $g_h = 0.508$  cm used a different version of the CFD solver, which resulted in different baseline levels. So, the fine-mesh baseline simulations were re-ran for every  $\alpha$  using that version. The simulated baseline  $h$  levels for  $g_h = 0.508$  cm are 29.9 W/(m<sup>2</sup>K), 45.6 W/(m<sup>2</sup>K), 67.4 W/(m<sup>2</sup>K), and 96.4 W/(m<sup>2</sup>K) for angles of attack of 0°, -4°, -8°, and -12°, respectively. The simulated baseline  $h$  levels for the three other gap heights are those listed in the previous paragraph. Figure 4.25 plots the maximum  $h$  level for every  $g_h$  as a function of  $\alpha$ . These maximum  $h$  levels are for the entire missile surface in the gap region. The maximum  $h$  levels occur off of the top centerline but are within one cylinder radius length from it. They do not exceed the maximum levels on the top centerline by more than 10%. For almost every case, maximum  $h$  levels increase with increasing  $g_h$ . The one exception is that for  $\alpha = -12^\circ$ , the maximum  $h$  level for  $g_h = 1.270$  cm is slightly below the one for  $g_h = 1.016$  cm. For  $g_h = 0.508$  cm, maximum  $h$  levels increase gradually with  $\alpha$ . For

$g_h = 0.762$  cm and  $g_h = 1.016$  cm, maximum  $h$  levels do not follow a monotonic trend with  $\alpha$ . For  $g_h = 1.270$  cm, the maximum  $h$  level for  $\alpha = -4^\circ$  is 45 times the baseline level, which is significantly above the maximum level for every other case. Maximum  $h$  levels measured by Neumann and Hayes are reproduced in Figure 4.26. They were measured at  $X/D = 0.3$  and were never above 11 times their baseline level.

Heating-contour plots for the missile and cylinder surfaces in the gap region were generated to visualize heating levels off of the top centerline. They are presented in Figures 4.27 and 4.28. Plots shown are for  $g_h = 0.762$  cm and  $\alpha = 0^\circ$ ,  $g_h = 1.016$  cm and  $\alpha = -12^\circ$ , and  $g_h = 1.270$  cm and  $\alpha = -4^\circ$ . The band of maximum heat transfer on the missile surface near  $X/D = 0.1$  is identifiable. Another region with high heat transfer is the upper half of the upstream side of the cylinder surface. When  $g_h = 0.762$  cm, the maximum  $h$  levels on the cylinder are similar to those on the missile surface. However, for the larger gap heights, the maximum  $h$  levels on the cylinder far exceed those on the missile surface. As shown in Figure 4.29, which plots the maximum  $h$  levels on the cylinder as a function of  $\alpha$ , the maximum  $h$  levels for the larger gap heights range from 40 to 100 times the baseline level. These levels are significantly above those on the missile surface, which range from 30 to 50 times the baseline level. The maximum  $h$  levels on the fin bottom surface were also checked, but were confirmed to never approach the maximum levels on the missile surface. In Figure 4.29, no results are shown for  $g_h = 0.508$  cm because the solution files for that gap height were outputted differently than for the others.

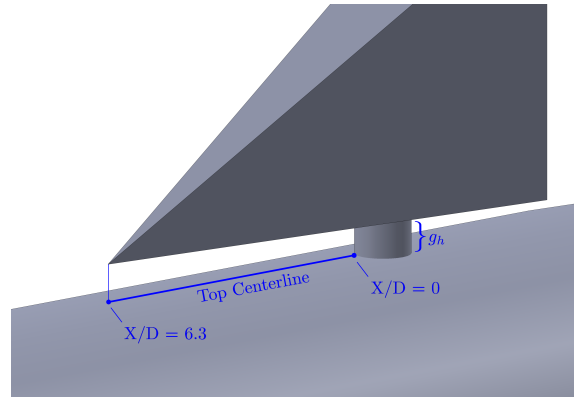


Fig. 4.1. Top centerline in gap region. Fin tip is located 6.3 cylinder diameter lengths upstream of the cylinder surface.

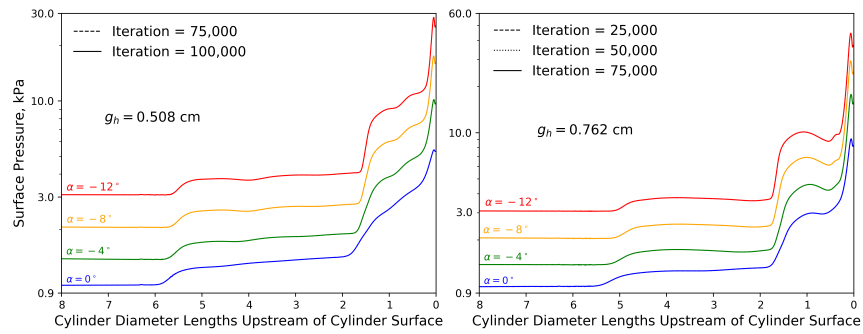


Fig. 4.2. Surface pressure on top centerline in gap region. Gap heights of 0.508 cm and 0.762 cm.

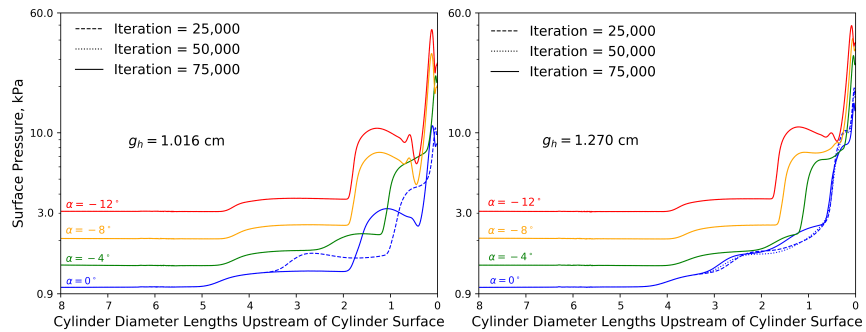


Fig. 4.3. Surface pressure on top centerline in gap region. Gap heights of 1.016 cm and 1.270 cm.

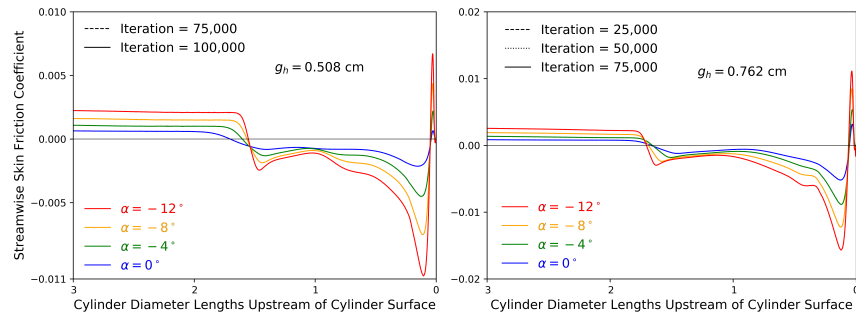


Fig. 4.4. Streamwise skin friction coefficient on top centerline in gap region. Gap heights of 0.508 cm and 0.762 cm.

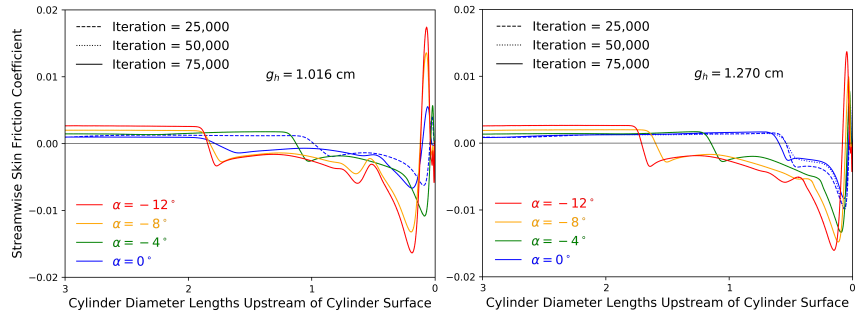


Fig. 4.5. Streamwise skin friction coefficient on top centerline in gap region. Gap heights of 1.016 cm and 1.270 cm.

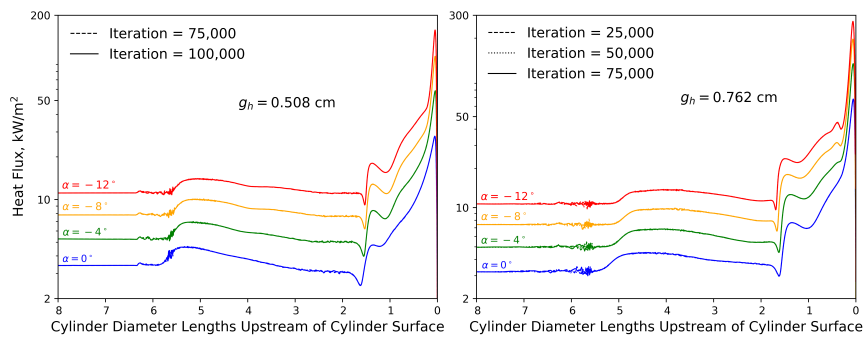


Fig. 4.6. Heat flux on top centerline in gap region. Gap heights of 0.508 cm and 0.762 cm.

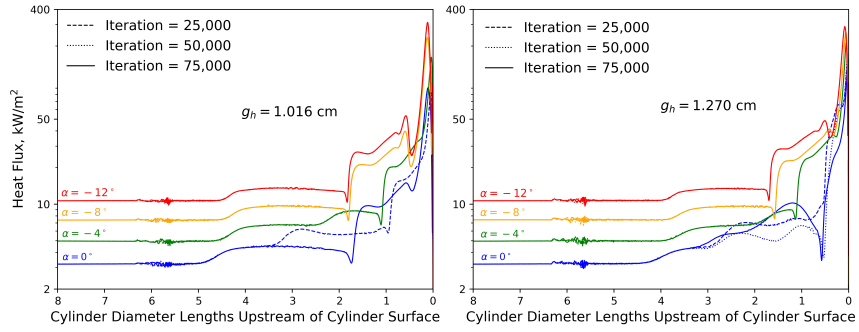


Fig. 4.7. Heat flux on top centerline in gap region. Gap heights of 1.016 cm and 1.270 cm.

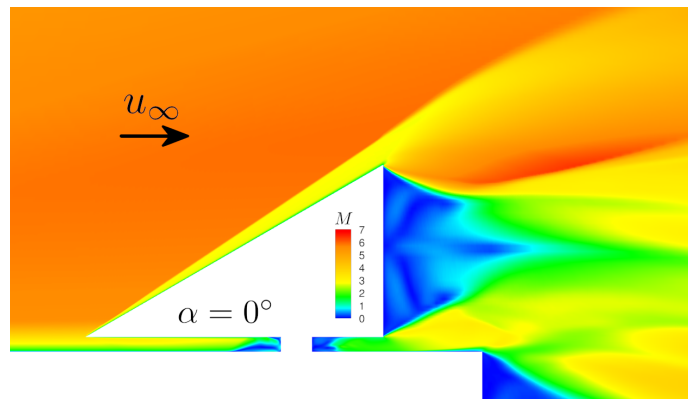


Fig. 4.8. Mach-contour plot of flow around fin region for a gap height of 0.762 cm and an angle of attack of  $0^\circ$ . Centerplane slice from 3D simulation.

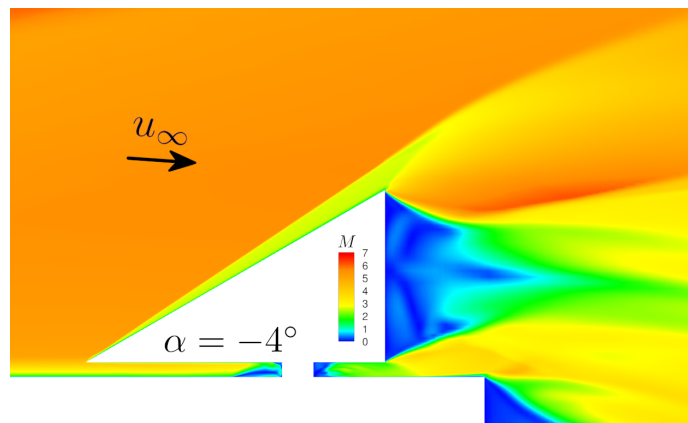


Fig. 4.9. Mach-contour plot of flow around fin region for a gap height of 0.762 cm and an angle of attack of  $-4^\circ$ . Centerplane slice from 3D simulation.

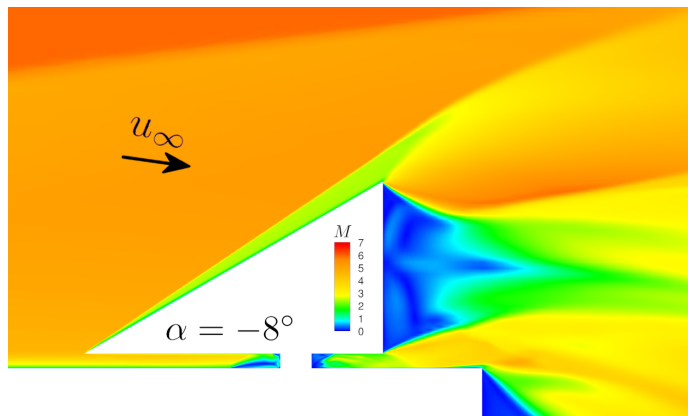


Fig. 4.10. Mach-contour plot of flow around fin region for a gap height of 0.762 cm and an angle of attack of  $-8^\circ$ . Centerplane slice from 3D simulation.

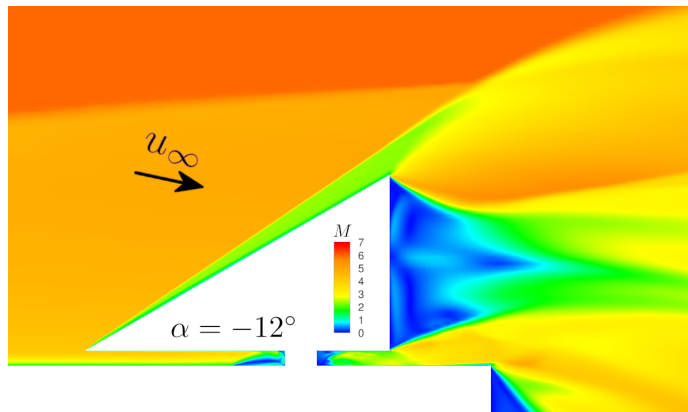


Fig. 4.11. Mach-contour plot of flow around fin region for a gap height of 0.762 cm and an angle of attack of  $-12^\circ$ . Centerplane slice from 3D simulation.

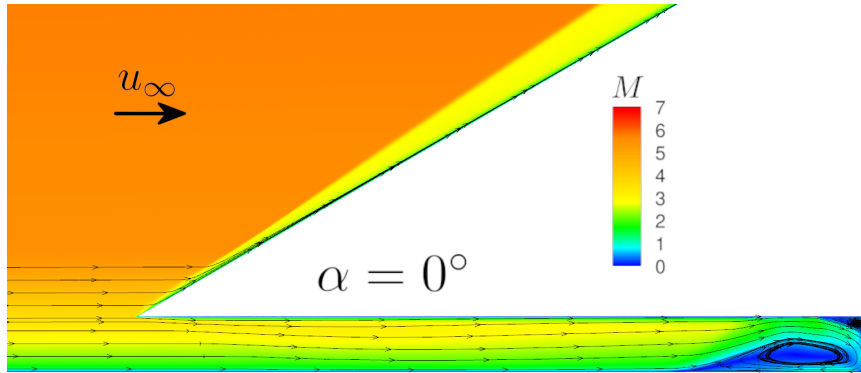


Fig. 4.12. Mach-contour plot with streamlines of flow in gap region for a gap height of 0.762 cm and an angle of attack of  $0^\circ$ . Centerplane slice from 3D simulation.

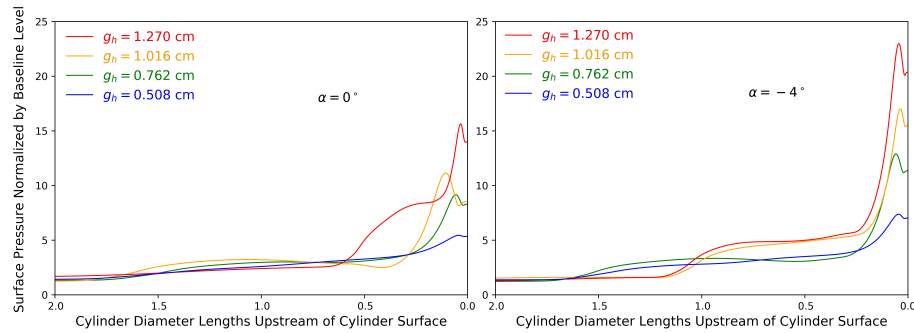


Fig. 4.13. Surface pressure on top centerline in gap region normalized by baseline level. Angles of attack of  $0^\circ$  and  $-4^\circ$ .

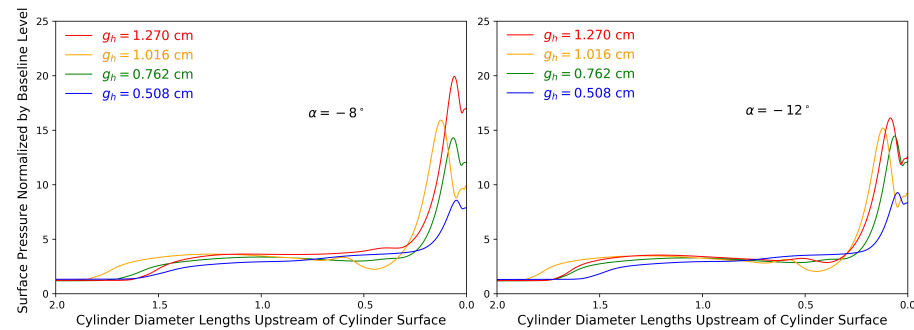


Fig. 4.14. Surface pressure on top centerline in gap region normalized by baseline level. Angles of attack of  $-8^\circ$  and  $-12^\circ$ .

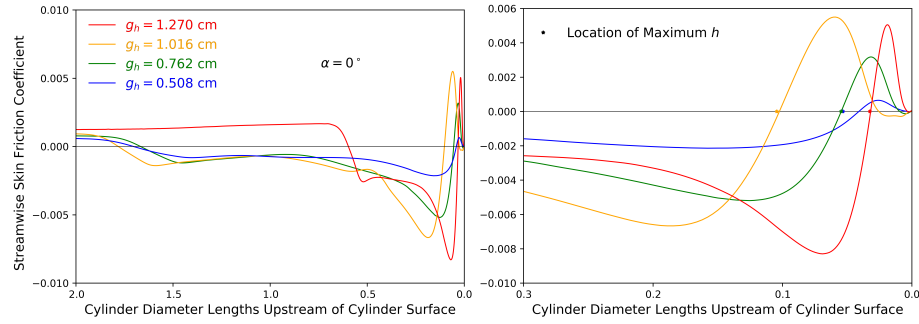


Fig. 4.15. Streamwise skin friction coefficient on top centerline in gap region for an angle of attack of  $0^\circ$ . Section very close to cylinder enlarged on right-hand side.

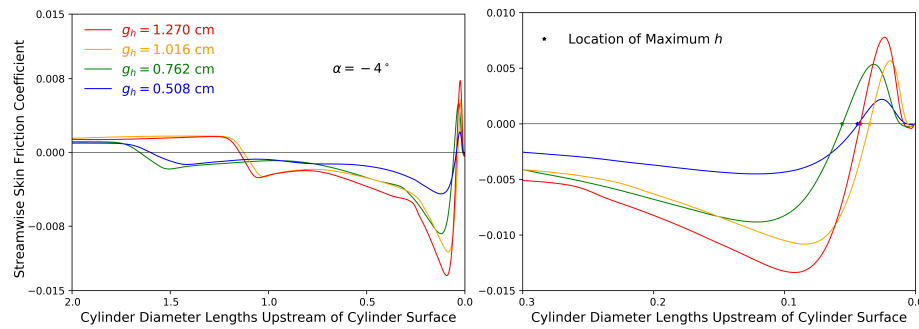


Fig. 4.16. Streamwise skin friction coefficient on top centerline in gap region for an angle of attack of  $-4^\circ$ . Section very close to cylinder enlarged on right-hand side.

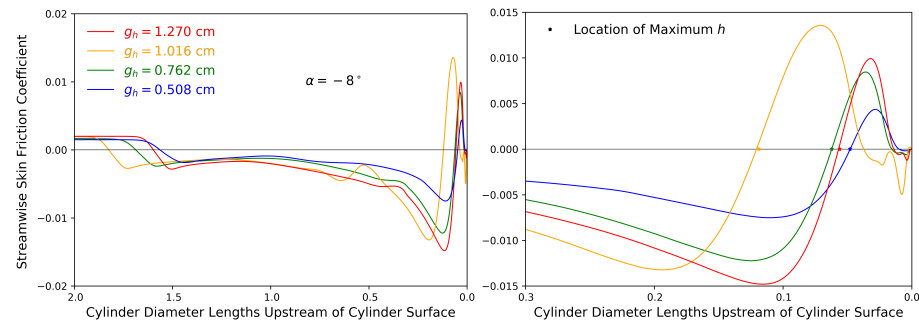


Fig. 4.17. Streamwise skin friction coefficient on top centerline in gap region for an angle of attack of  $-8^\circ$ . Section very close to cylinder enlarged on right-hand side.

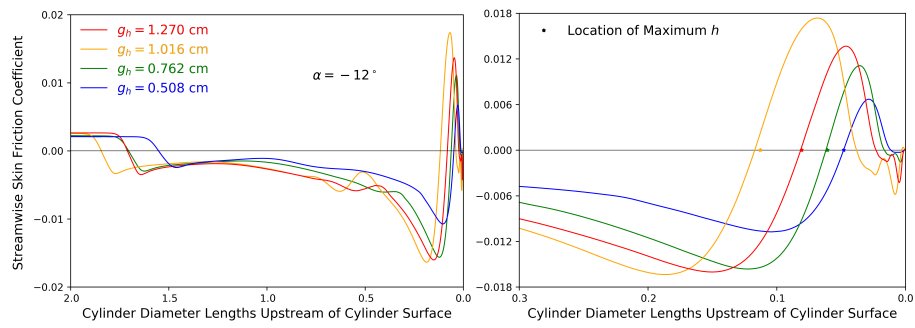


Fig. 4.18. Streamwise skin friction coefficient on top centerline in gap region for an angle of attack of  $-12^\circ$ . Section very close to cylinder enlarged on right-hand side.

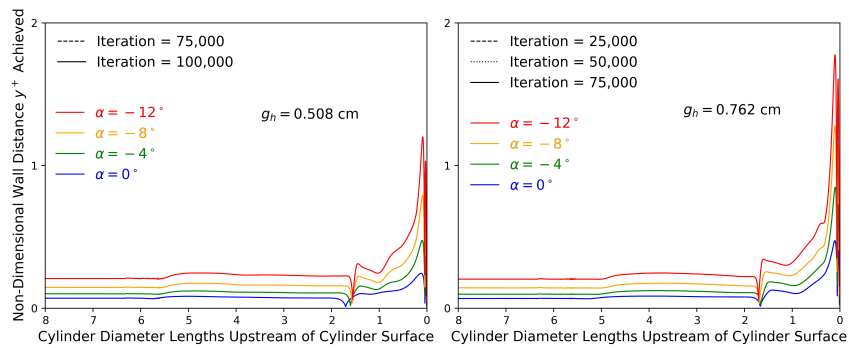


Fig. 4.19. Achieved  $y^+$  on top centerline in gap region for gap heights of 0.508 cm and 0.762 cm.

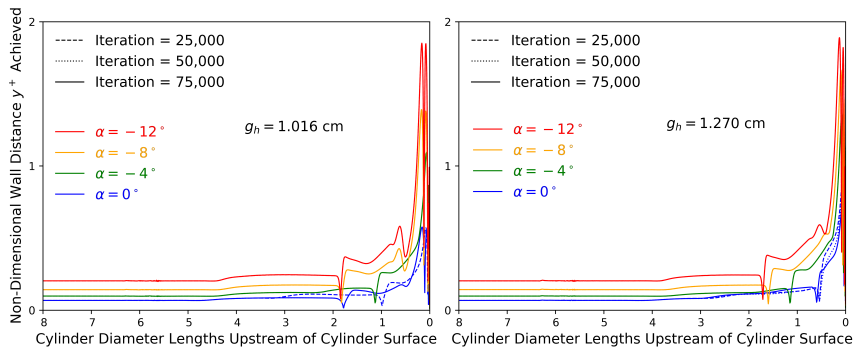


Fig. 4.20. Achieved  $y^+$  on top centerline in gap region for gap heights of 1.016 cm and 1.270 cm.

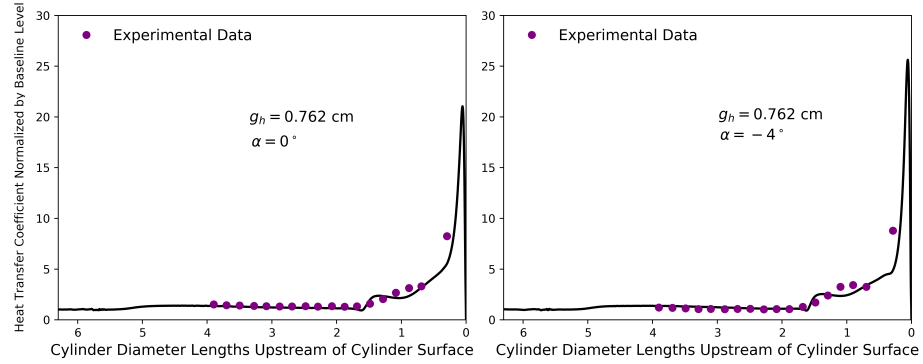


Fig. 4.21. Heat transfer coefficient normalized by baseline level on top centerline in gap region. Gap height of 0.762 cm and angles of attack of  $0^\circ$  and  $-4^\circ$ . Black lines are simulated distributions.

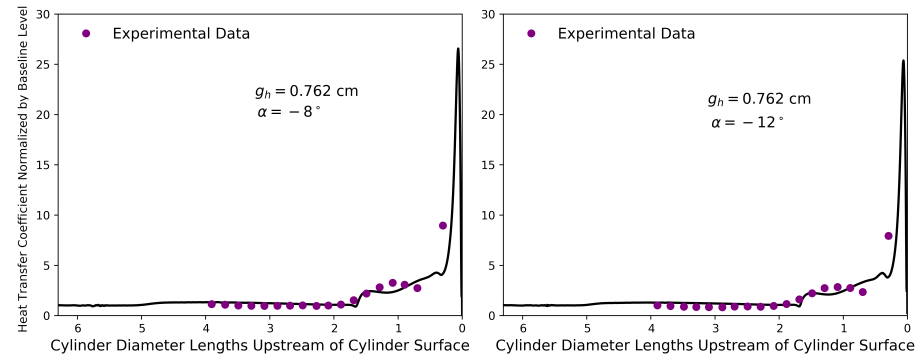


Fig. 4.22. Heat transfer coefficient normalized by baseline level on top centerline in gap region. Gap height of 0.762 cm and angles of attack of  $-8^\circ$  and  $-12^\circ$ . Black lines are simulated distributions.

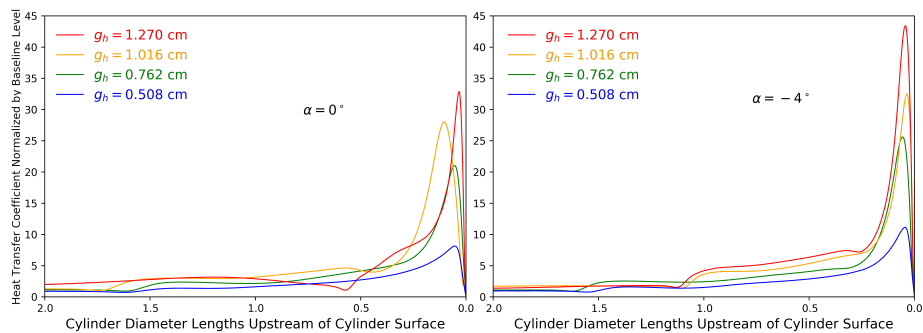


Fig. 4.23. Heat transfer coefficient normalized by baseline level on top centerline in gap region. Angles of attack of  $0^\circ$  and  $-4^\circ$ .

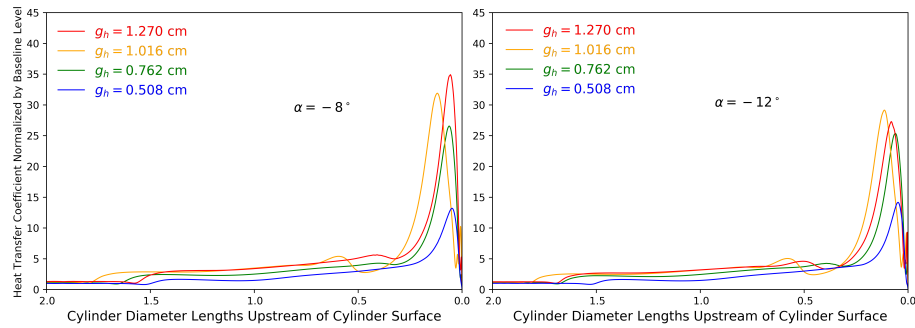


Fig. 4.24. Heat transfer coefficient normalized by baseline level on top centerline in gap region. Angles of attack of  $-8^\circ$  and  $-12^\circ$ .

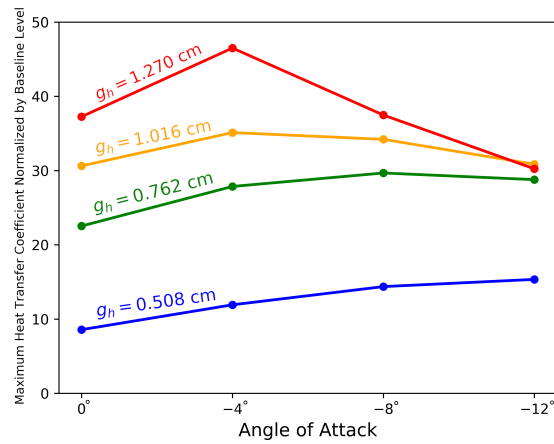


Fig. 4.25. Maximum heat transfer coefficient on missile surface normalized by baseline level as function of  $\alpha$ .

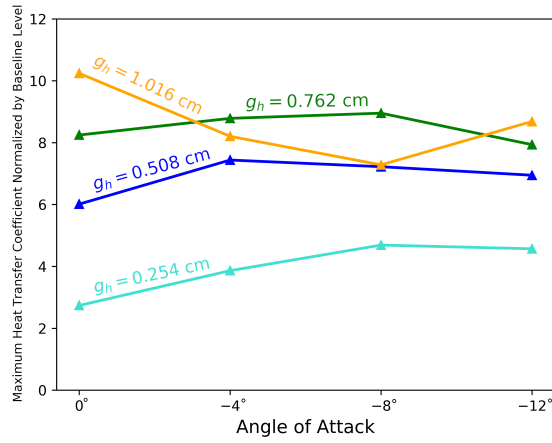


Fig. 4.26. Maximum heat transfer coefficient on missile surface normalized by baseline level as function of  $\alpha$ . Measured by Neumann and Hayes at  $X/D = 0.3$ . From their Figure 6.11 [8].

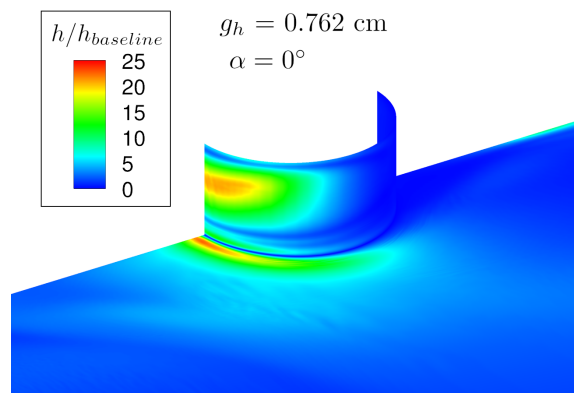


Fig. 4.27. Heating-contour plot normalized by baseline level on missile and cylinder surfaces for a gap height of 0.762 cm and an angle of attack of  $0^\circ$ .

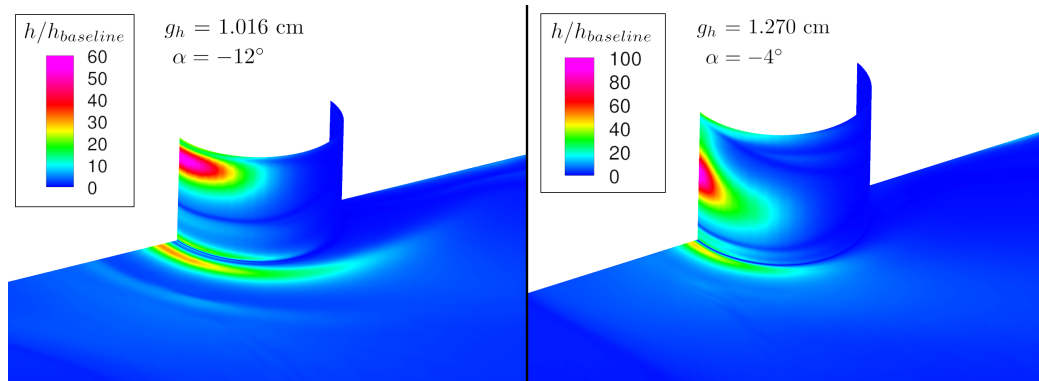


Fig. 4.28. Heating-contour plot normalized by baseline level on missile and cylinder surfaces. Case for gap height of 1.016 cm and an angle of attack of  $-12^\circ$  and case for gap height of 1.270 cm and an angle of attack of  $-4^\circ$ .

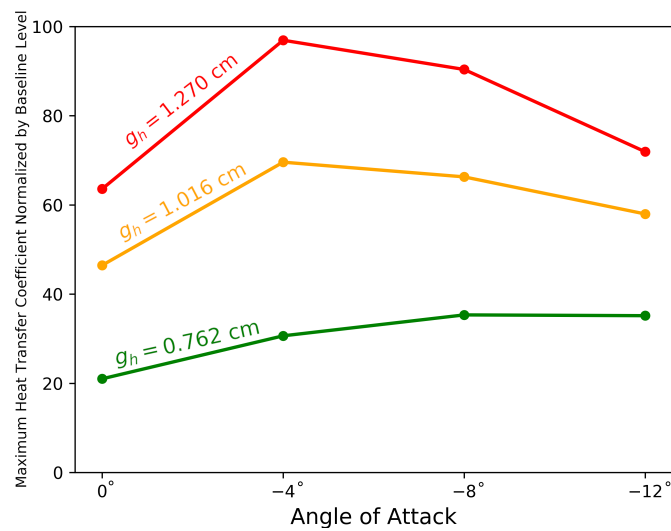


Fig. 4.29. Maximum heat transfer coefficient on cylinder surface normalized by baseline level as function of  $\alpha$ .

## 5. CONCLUSIONS

This research involved the study of Mach 6 flow over a missile model configuration with and without an attached fin. Simulated results for various properties were analyzed and compared to measurements from wind tunnel tests. Beyond replicating experimental data, this thesis aimed to expand understanding of heating in the gap region between the missile and fin. This chapter outlines the main conclusions drawn from analyzing the simulated results, as well as recommendations for future study.

Simulated properties of the baseline configuration agreed very well with experimental data. All heat transfer coefficient and surface pressure calculations on the windward side, for every simulated angle of attack, fell within ranges of measured values from the wind tunnel tests conducted by Neumann and Hayes [8]. Levels of these properties on the top centerline were shown to increase with increasing angle of attack, as measured. Furthermore, simulated Pitot pressure profiles of the boundary layer and shock wave over the top centerline agreed well with experimental data points. The fine mesh predicted the location of the shock wave front most closely, affirming the importance of grid quality near shock waves. The boundary layer on the top centerline was calculated to decrease in thickness with increasing  $\alpha$ , as was also measured.

Simulated properties of the missile-fin configuration were organized by a parametric study that involved variations in angle of attack and the gap height between the missile and fin. Levels of surface pressure and heat transfer were normalized by each angle of attack's baseline level. As gap height increased, calculated normalized maximum levels of surface pressure and heat transfer almost always increased. Variations in angle of attack did not affect normalized maximum levels monotonically across gap heights. Neumann and Hayes's measurements of normalized maximum heat transfer coefficients also generally increased with gap height and did not follow a monotonic

trend with angle of attack. Skin friction and streamline calculations support the existence of a SWBLI in the gap region within two cylinder diameter lengths upstream of the cylinder surface. The recirculation region present in this interaction was calculated to cause a spike in surface pressure, as large as 20 times the baseline level, and heat transfer, as large as 45 times the baseline level, near its reattachment point very close to the cylinder. Neumann and Hayes also reported that an interaction exists in this region by writing that “[t]he interaction was found to extend about two diameters upstream of the torque tube with the peak heating location being no more than 0.3 diameters upstream” [8]. Their closest thermocouple to the cylinder was located at  $X/D = 0.3$ .

Maximum heat transfer coefficients on the top centerline were calculated to occur within 0.1 cylinder diameter lengths upstream of the cylinder surface. They ranged from 10 times the baseline level for  $g_h = 0.508$  cm to over 40 times the baseline level for  $g_h = 1.270$  cm. These levels are significantly higher than those measured by Neumann and Hayes at  $X/D = 0.3$ , which were 2 to 11 times the baseline level for gap heights up to 1.016 cm. Furthermore, the maximum simulated heat transfer levels on the missile surface were not located exactly on the top centerline. They were located adjacent to the top centerline, but by no more than one cylinder radius length, and were only higher than the maximum levels on the top centerline by less than 10%. However, simulated heat transfer levels on the upstream side of the cylinder far exceeded those on the missile surface. The maximum heat transfer levels on the cylinder surface for the larger gap heights were calculated to range from 40 to 100 times the baseline level. Given that the maximum heat transfer levels simulated on the missile surface were 30 to 50 times the baseline level, the cylinder surface may be an important design point. Neumann and Hayes concluded that the region under the fin and upstream of the cylinder is the “design point for the thermal protection of gapped control surfaces.” Simulated maximum heat transfer levels on the missile surface, being more severe than those measured, support that conclusion. Yet, the simulations calculated more intense heating on the upstream side of the cylinder surface, which was not analyzed

in the wind tunnel tests. Based on the simulations, the design points for thermal protection in the gap region are both the missile surface directly upstream of the cylinder and the upstream side of the cylinder surface.

The missile-fin configuration offers many avenues for additional study. Since Neumann and Hayes took measurements for nonzero roll angles, incorporating various roll angles in the parametric study would expand the set of results available for comparison. Additionally, trends could be better identified with many more angles of attack and gap heights simulated. However, the grid generation approach used for this research does not enable easy changes in geometry. It also inflates point counts because the grid density in the gap region propagates to other regions of the domain. A potential solution would be to use an overset mesh for future simulations of the missile-fin configuration. This approach would likely reduce point counts and enable the gap height to be easily adjusted. Research that incorporates these recommendations would produce a large amount of results that would contribute to the understanding of the effects of shock wave/boundary layer interactions in gap regions.

## REFERENCES

- [1] J. D. Anderson, *Hypersonic and High Temperature Gas Dynamics*, 2nd ed. Reston, VA: American Institute of Aeronautics and Astronautics, Inc., 2006, pp. 261, 271, 309, 292, 299.
- [2] E. J. Hopkins, E. R. Keener, and T. E. Polek, "Hypersonic Turbulent Skin-Friction and Boundary-Layer Profiles on Nonadiabatic Flat Plates," *AIAA Journal*, vol. 10, no. 1, pp. 40–48, Jan 1972.
- [3] M. E. Tauber, "A Review of High-Speed, Convective, Heat-Transfer Computation Methods," National Aeronautics and Space Administration, Office of Management, Tech. Rep. 2914, 1989.
- [4] J. Détery, J. G. Marvin, and E. Reshotko, "Shock-Wave Boundary Layer Interactions," Advisory Group for Aerospace Research and Development Neuilly-Sur-Seine (France), Tech. Rep. 280, 1986.
- [5] D. V. Gaitonde, "Progress in Shock Wave/Boundary Layer Interactions," *Progress in Aerospace Sciences*, vol. 72, pp. 80–99, 2015.
- [6] E. R. van Driest, "The Problem of Aerodynamic Heating," *Aeronautical Engineering Review*, vol. 15, pp. 26–41, 1956.
- [7] K. H. Gruenewald, "Temperature Recovery Factors in the Transitional and Turbulent Boundary Layer on a 40-degree Cone Cylinder at Mach Number 2.9," Naval Ordnance Lab, White Oak, MD, Tech. Rep. 2742, 1953.
- [8] R. D. Neumann and J. R. Hayes, "Aerodynamic Heating in the Fin Interaction Region of Generalized Missile Shapes at Mach 6," Air Force Flight Dynamics Laboratory Wright-Patterson, OH, Tech. Rep. 79-3066, 1979.
- [9] J. D. Anderson, *Modern Compressible Flow with Historical Perspective*, 3rd ed. New York, NY: McGraw-Hill New York, 2003, pp. 80, 86.
- [10] S. M. Yahya, *Fundamentals of Compressible Flow: SI Units with Aircraft and Rocket Propulsion*, 3rd ed. New Age International, 2003, p. 185.
- [11] "Pointwise ver. 18.3," Pointwise Inc., fort Worth, TX.
- [12] F. M. White, *Fluid Mechanics*, 7th ed. New York, NY: McGraw-Hill New York, 2011, p. 473.
- [13] R. L. Sorenson, "The 3DGRAPE Book: Theory, Users' Manual, Examples," National Aeronautics and Space Administration, Moffett Field, CA, Tech. Rep. NASA-TM-102224, 1989.

- [14] “T-Rex Hybrid Meshing in Pointwise,” Pointwise Inc., 2011, [Online]. Available: <https://www.pointwise.com/theconnector/2011-July/T-Rex-Hybrid-Meshing-Pointwise.html>.
- [15] D. R. McDaniel, T. R. Tuckey, and S. A. Morton, “The HPCMP CREATE™-AV Kestrel Computational Environment and its Relation to NASA’s CFD Vision 2030,” in *55th AIAA Aerospace Sciences Meeting*, no. AIAA 2017-0813, 2017.
- [16] B. van Leer, “Flux-Vector Splitting for the Euler Equations,” ICASE Report 82-30, Tech. Rep., 1982.
- [17] T. J. Barth and D. C. Jespersen, “The Design and Application of Upwind Schemes on Unstructured Meshes,” in *27th Aerospace Sciences Meeting*, no. AIAA 1989-366, 1989, p. 366.
- [18] P. Spalart and S. Allmaras, “A One-Equation Turbulence Model for Aerodynamic Flows,” in *30th Aerospace Sciences Meeting and Exhibit*, no. AIAA 1992-439, 1992.
- [19] R. W. Tramel, R. H. Nichols, and P. G. Buning, “Addition of Improved Shock-Capturing Schemes to OVERFLOW 2.1,” in *19th AIAA Computational Fluid Dynamics Conference*, no. AIAA-2009-3988, 2009.
- [20] “Cray XC40 (Excalibur) User Guide,” ARL DSRC, [Online]. Available: <https://www.arl.hpc.mil/docs/excaliburUserGuide.html>.
- [21] I. A. Hall, “Simulating Scramjet Behavior: Unstart Prediction in a Supersonic, Turbulent Inlet-Isolator Duct Flow,” Master’s thesis, Purdue University, West Lafayette, 2019.
- [22] “Tecplot 360 ex, software package, ver. r,” Tecplot, Inc., Bellevue, WA.
- [23] F. M. White, *Viscous Fluid Flow*, 3rd ed. New York, NY: McGraw-Hill New York, 2006, pp. 28, 486.
- [24] M. Atkinson, J. Poggie, and J. Camberos, “Hypersonic flow computations for an elliptic cone at high angle of incidence,” *Journal of Spacecraft and Rockets*, vol. 49, no. 3, pp. 496–506, 2012.
- [25] E. W. Lemmon, , I. H. Bell, M. L. Huber, and M. O. McLinden, “NIST National Institute of Standards and Technology Chemistry WebBook SRD 69,” 2020. [Online]. Available: <https://webbook.nist.gov/chemistry/fluid/>

## APPENDIX

### A. MODEL DIMENSIONED DRAWINGS

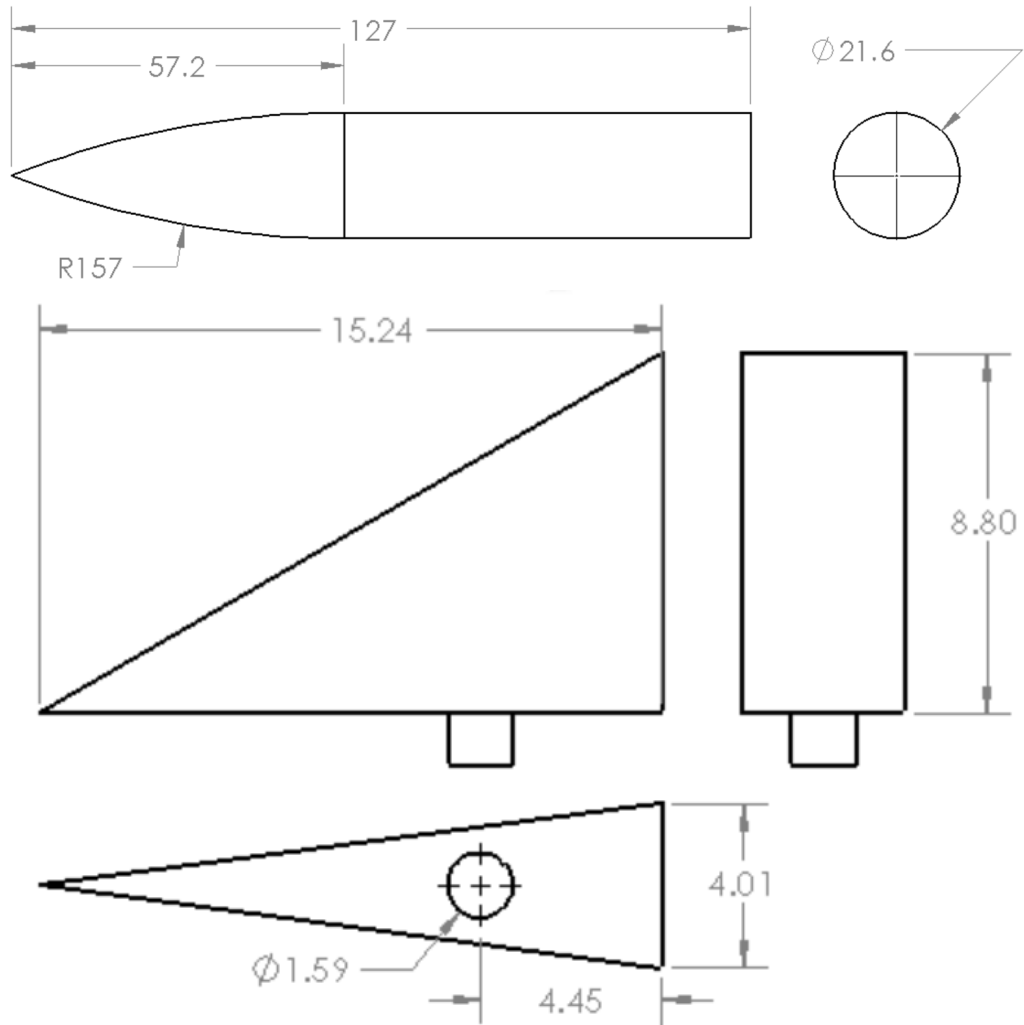


Fig. A.1. Dimensions of simulated missile and fin models. Units cm.

## B. DERIVATION OF EQUATION 2.4

$$y^+ = \frac{\rho u \Delta s}{\mu} \sqrt{\frac{C_f}{2}} \quad (\text{Definition of } y^+) \quad (\text{B.1})$$

$$\Delta s(y^+ = 1) = \frac{1}{Re_\infty} \sqrt{\frac{2}{C_f}} \quad (\text{Using freestream unit Reynolds number}) \quad (\text{B.2})$$

$$C_f \approx \frac{0.027}{Re_\infty^{1/7}} \quad (\text{Approximation from turbulent flat plate boundary layer theory [12]}) \quad (\text{B.3})$$

$$\Delta s = 8.61 Re_\infty^{-13/14} \text{ m} \quad (\text{Gathering exponents and rounding}) \quad (\text{B.4})$$

### C. STAGNATION POINT HEATING

For comparison to values obtained in the computations, an estimate can be made for the laminar stagnation point heat flux on a cylinder perpendicular to the flow for the experimental conditions. The correlation [1] based on numerical solutions presented by Anderson is

$$q_w = 0.57Pr^{-0.6}(\rho_e\mu_e)^{1/2}\sqrt{\frac{1}{R}\sqrt{\frac{2(P_e - P_\infty)}{\rho_e}}}(h_R - h_w) \quad (\text{C.1})$$

where  $q_w$  is heat flux,  $Pr$  is Prandtl number, subscript  $e$  refers to boundary layer edge,  $R$  is cylinder radius,  $h_R$  is recovery enthalpy, and  $h_w$  is enthalpy at the stagnation point. The recovery enthalpy can be found using

$$h_R = h_e + r(h_0 - h_e) \quad (\text{C.2})$$

where  $r$  is the recovery factor and  $h_0$  is the stagnation enthalpy outside of the boundary layer. By assuming a calorically perfect gas,  $q_w$  can be calculated using the freestream flow conditions from this thesis. Normal shock wave relations [9] are used to find boundary layer edge properties from freestream properties. Sutherland's law [1] is used to calculate  $\mu_e$  from  $T_e$ . All  $h$  values are calculated using  $C_pT$  where  $C_p = R_{gas}(1 - \gamma^{-1})^{-1}$  for a calorically perfect gas. The specific gas constant  $R_{gas}$  is 287.058 J/(kgK) and  $\gamma$  is 1.4. A recovery factor of 0.834 was obtained as a function of Mach number [1]. The Prandtl number  $Pr$  was calculated using average  $\mu$  between the wall and boundary layer edge. It also involved the thermal conductivity of air found from National Institute of Standards and Technology (NIST) online database [25] for air at average  $T$  and  $P$  between the wall and boundary layer edge.

For the freestream conditions, cylinder diameter, and wall temperature used in this thesis,  $q_w = 86 \text{ kW/m}^2$ . The corresponding  $h$  using a  $T_{ref}$  of  $0.9T_{0\infty}$  is  $750 \text{ W/(m}^2\text{K)}$ .